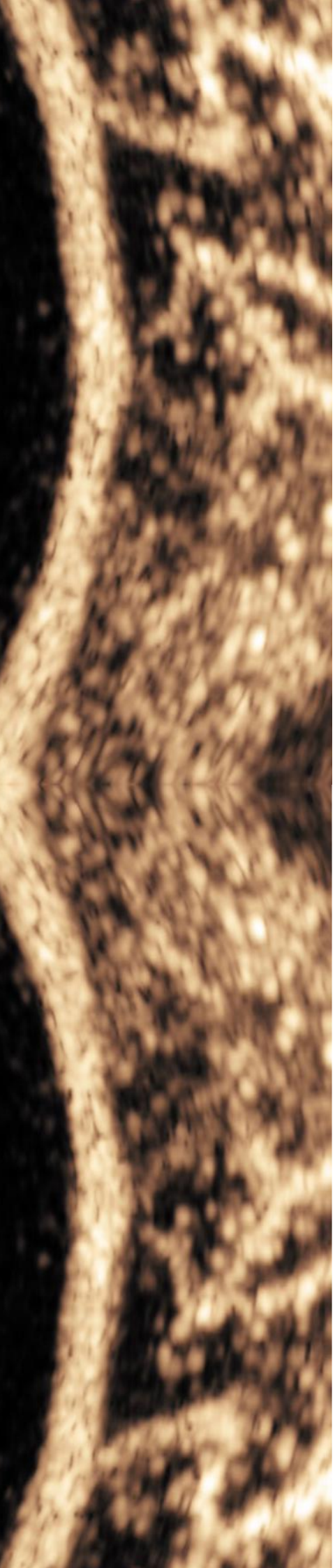

Master Thesis

Real-time analysis of Dynamic Contrast Enhanced Ultrasound for catheter position optimisation in Transarterial Radioembolisation

Adrie Visser

Faculty of Science & Technology
Biomedical Engineering

Multi-Modality Medical Imaging Group

Graduation Committee:
Prof. Dr. S. Manohar
Dr. E. Groot Jebbink
Ir. J.L. van der Hoek
Prof. Dr. Ir. C.L. de Korte

February 14th, 2024

Thesis submitted by
Adrie Visser
under the supervision of
Prof. Dr. S. Manohar,
Dr. E. Groot Jebbink,
Ir. J.L. van der Hoek,
in order to fulfil the necessary requirements to obtain a Master's degree in
Biomedical Engineering at the University of Twente
and defended on
Wednesday, 14th of February, 2024

UNIVERSITY OF TWENTE. | TECHMED CENTRE

List of Abbreviations

CPS	Contrast Pulse Sequence
CT	Computed Tomography
DCE-US	Dynamic Contrast Enhanced Ultrasound
DR	Dynamic Range
HCC	Hepatocellular carcinoma
^{165}Ho	Holmium-165
^{166}Ho	Holmium-166
MRI	Magnetic Resonance Imaging
PI	Peak Intensity
RF	Radio Frequency
ROI	Region Of Interest
SPECT	Single Photon Emission Computed Tomography
^{99m}TC-MMA	Technetium-99m Macro Aggregated Albumin
TIC	Time Intensity Curve
TARE	Transarterial Radioembolisation
^{90}Y	Yttrium-90
US	Ultrasound

Table of Contents

Chapter 1 | Introduction

Globally, primary liver cancer is the third most common cause of cancer deaths, with approximately 900,000 new cases and 830,000 deaths each year, worldwide [1]. Hepatocellular carcinoma (HCC) is the predominant type, accounting for over 90% of all cases. Surgical resection and liver transplantation are the two standard curative options for HCC [2]. However, more than 70% of the patients are ineligible for these treatments due to poor liver function, limited hepatic regenerative capacity or metastases at advanced stages. Therefore, the major patient group is treated with palliative care [3].

One treatment option for unresectable liver tumours is called transarterial radioembolisation (TARE), which is performed over 20.000 times annually, worldwide [4]. While the treatment is inherently palliative, it has the potential to facilitate the path for curative treatments [5]. Microspheres filled with a radioactive isotope are injected via a microcatheter into the hepatic arterial vasculature. The microspheres embolise in the capillary beds downstream, locally targeting tissue with a high dose of beta radiation and closing off the blood supply to the tumour [5]. The treatment relies on the dual blood supply of the liver. Hepatic tumours are for 95% supplied by arterial flow, whereas healthy tissue is perfused by hepatic arteries and the portal vein with a 1:4 ratio. As a result, the radiation dose of the healthy tissue is naturally lowered [6]. The median overall survival of TARE is related to the tumour-absorbed dose and varies widely, from months to over a year. The treatment is more effective if the dose received by the tumour is higher. In order to improve the efficiency of the treatment, the microsphere deposition at the tumour location should therefore be optimised [7].

In the current approach, a separate work-up procedure is conducted prior to the final treatment for planning and the exclusion of contraindication [5]. During the work-up, preparatory angiography and cone-beam Computed Tomography (CT) scans are used to choose the injection position for the final treatment based on the hepatic vasculature map and contrast enhancement in- and outside the target region. A scout injection is performed at the marked position with small amounts of holmium-166 (^{166}Ho) or technetium-99m macroaggregated albumin (^{99m}TC-MMA) as surrogate radioactive markers. Subsequently, the distribution of these markers within and outside the liver is assessed based on Single Photon Emission Computed Tomography (SPECT) in combination with CT, or Magnetic Resonance Imaging (MRI) for ^{166}Ho. If the results of the work-up are acceptable, the final treatment is conducted [5].

A considerable limitation of the current approach is the difficulty of reproducing the scout injection during the final treatment [8]. In addition to hemodynamic conditions and injection velocity, the positioning of the catheter has great influence on the microsphere distribution, with a possible difference up to 40%, by an axial position variation of only 5 mm [9]. Currently, there is lack of feedback on the catheter position in terms of lateral and axial location, as well as angulation of the catheter tip [4]. The absence of feedback during the treatment leads to suboptimal results and risk of unpredicted off-side toxicity [10]. An example is shown in Figure 1.

An alternative TARE procedure with real-time feedback might offer more control over the microsphere distribution. The resulting microsphere distribution could be estimated by injecting microbubbles as surrogate particles, as these two particles have shown to follow similar trajectories [11]. With dynamic contrast enhanced ultrasound (DCE-US), microbubble presence in tissue can be visualised and quantitively analysed using time intensity curves (TICs) [12]. Based on real-time analyses of the microbubble concentrations in the Region Of Interest (ROI), resulting from microbubble injections at various locations, the optimal catheter position to target the tumour could be determined. The goal of this thesis is to develop a DCE-US guided TARE protocol, with the goal to provide the user with real-time feedback on the catheter position and to improve the microsphere deposition at the tumour location.

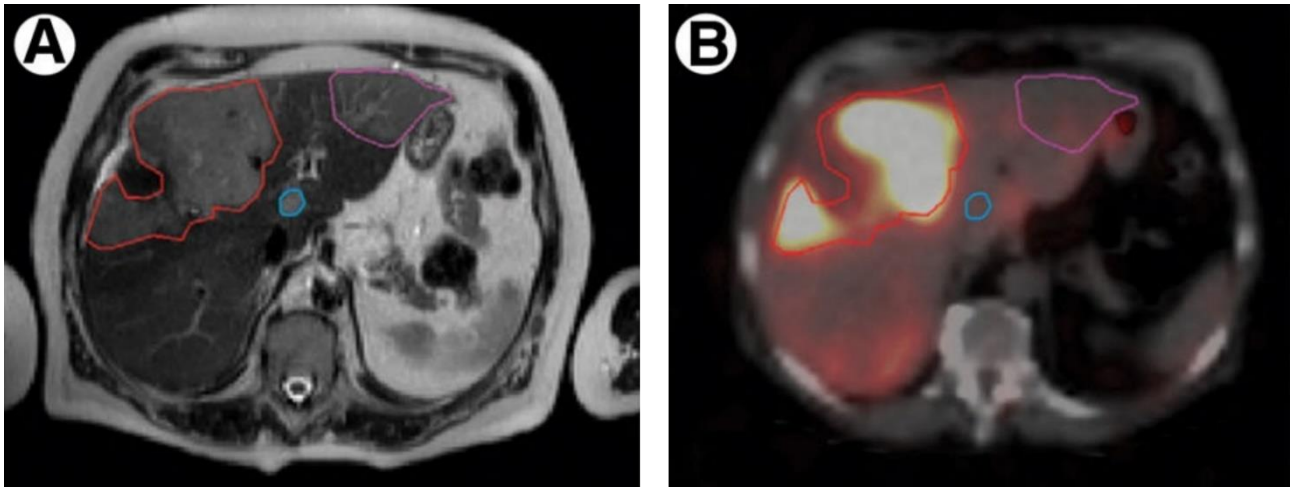

a. **b.**

Figure 1. Example of suboptimal treatment results. a.T2-weighted MRI-scan indicating 3 tumour sides before TARE, in the coloured regions **b**. SPECT-CT after treatment, the two regions on the right clearly received a suboptimal dose. Reprinted, from Smits et al. (2012) [10].

Based on the project goal, the following research question is formulated: "How can the catheter position for TARE be optimised using DCE-US with real-time analyses of TICs of the microbubble distribution in an ROI in an ex-vivo perfused porcine liver. To answer this question, the following sub-questions are explored:

- How can we perform DCE-US on an ex-vivo perfused porcine liver?
- How can we analyse the information in DCE-US scans?
- How can we use the result of this TIC analysis to optimise the catheter position during the TARE procedure?
- How can we do this real-time?
- How can we integrate this in an augmented TARE procedure?

Following this introduction, the report is segmented into two chapters: the first chapter contains background information and the second chapter a paper. The answers to the first three sub-questions can be found in the background chapter. The outcomes related to the last two sub-questions and the main question are provided in the paper. Additional details and process descriptions can be found in the appendices.

Chapter 2 | Background

In this chapter, background information will be provided to familiarise the reader with recurring concepts in the remainder of this thesis. Besides, the answers to the first three sub-questions can be found in the second paragraph of this chapter. These findings were essential for determining the approach taken to answer the remaining questions.

2.1 Transarterial Radioembolisation

TARE is a selective intra-arterial procedure, currently used as a palliative treatment for patients with unresectable liver tumours [13], [14]. Other names for the treatment are Selective Internal Radiation Therapy or radioembolisation. The goal of the treatment is to selectively target the tumour with a high dose of radiation, while preserving the healthy parenchyma. Through an arterial-inserted microcatheter, the arteries supplying the tumour are targeted with microspheres filled with an β-emitting radioactive isotope: yttrium-90 (^{90}Y) or ^{166}Ho, which also emits gamma radiation. Because of their size, the microspheres will embolise the capillaries downstream, blocking the blood flow to the tumour and locally target the tissue with a high radiation dose, see Figure 2 [15].

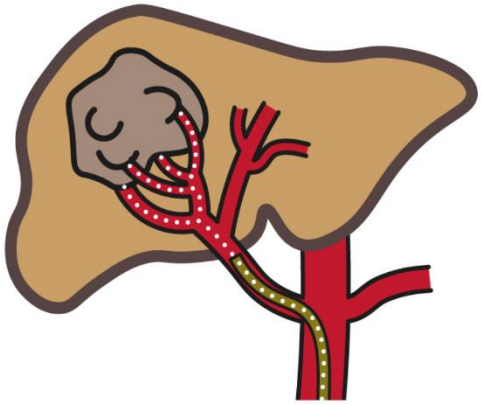

Figure 2. Schematic overview of the TARE procedure. The microspheres, shown in white, are injected through a catheter, shown in yellow. Reprinted, with permission from Groot Jebbink (2020) [4].

In this treatment, the unique blood supply of the liver is utilised: healthy liver tissue is perfused for 25% by the hepatic artery and the other 75% is supplied by the portal vein. In contrast, liver tumours are supplied for 95% by the hepatic artery [6], [15]. As a result, by administering microspheres into the hepatic artery, tumours can be selectively treated without excessively damaging the healthy tissue [15].

The TARE treatment consists of two stages: a work-up procedure and the final treatment. Both procedures are performed by interventional radiologists and take roughly an hour and a half [13]. The work-up procedure is a trial of the final treatment and is used for planning and exclusion of contraindication. Under ultrasound guidance, a microcatheter is placed in the femoral artery, which is then threaded up to the hepatic artery [16]. The target location for the catheter is determined based on contrast cone-beam CT and, based on angiography, the catheter is navigated through the liver vasculature. The contrast fluid needed for these images is injected through the catheter. The CT images show the tumour location with respect to the 3D arterial vasculature of the liver. Based on this information, it is estimated which artery predominantly perfuses the tumour and as a result, where the catheter should be placed ideally. Subsequently, efforts are made to maneuver the catheter to this position. However, angulation and spasms of the arteries might obstruct the advancement of the catheter.

When an acceptable position is reached, a new contrast CT is performed. Based on the ratio of the contrast enhancement inside and outside the potential tumour perfusing artery, it is decided if the position is sufficient

or not. In case this ratio is not sufficient, an alternative position is chosen, and the process is repeated. Once the catheter position is acceptable, a scout injection is performed with small amounts of ^{166}Ho or ^{99m}Tc-MMA as surrogate radioactive markers.

The resulting distribution of the markers can only be assessed after the work-up procedure. Evaluation is performed by means of MRI or SPECT/CT. The distribution is evaluated based on multiple characteristics. One of these is the ratio of radiated liver volume to non-radiated liver volume. Furthermore, the ratio of radiation uptake between tumoral and healthy tissue is considered. Moreover, the fraction of the markers which ended up outside the liver is taken into account [17]. If the overall result is acceptable, the final treatment can be performed.

The final treatment is performed a couple of weeks later. Ideally, the catheter should be positioned exactly at the location determined by the work-up procedure. An effort is made to replicate this position as good as possible based on angiography, and the treatment dose of embolising microspheres filled with a radioactive isotope is injected. The treatment is evaluated through multiple CT or MRI scans conducted in the weeks following the treatment [7]. A higher tumour radiation-absorbed dose results in an improved median overall survival [7].

2.2. Dynamic Contrast Enhanced Ultrasound

This section will provide the reader with background information needed to understand the challenges and choices regarding the use of DCE-US for the optimalisation of the catheter position during the TARE procedure.

2.2.1. Current usage

DCE-US is a non-invasive technique which can be used for the real-time visualisation of perfusion, by combining microbubble contrast agents and a conforming US pulsing scheme. Additionally, the US signal over time is converted to a TIC for the quantification of the perfusion, see Figure 3. The first clinical application was in the early 2000s and the technique has been further developed since, with some breakthroughs being the improvement of the stability of the microbubbles, updates of DCE-US guidelines and the ease of operation [18]. The current clinical usage includes tracking the tumour treatment response, evaluation of carotid disease and tumour staging [19], [20], [21]. In ex-vivo research, experiments on pig livers show the suitability of DCE-US for the advancement of drug delivery-based interventions, since it can localise drug release by quantifying microbubble destruction [22].

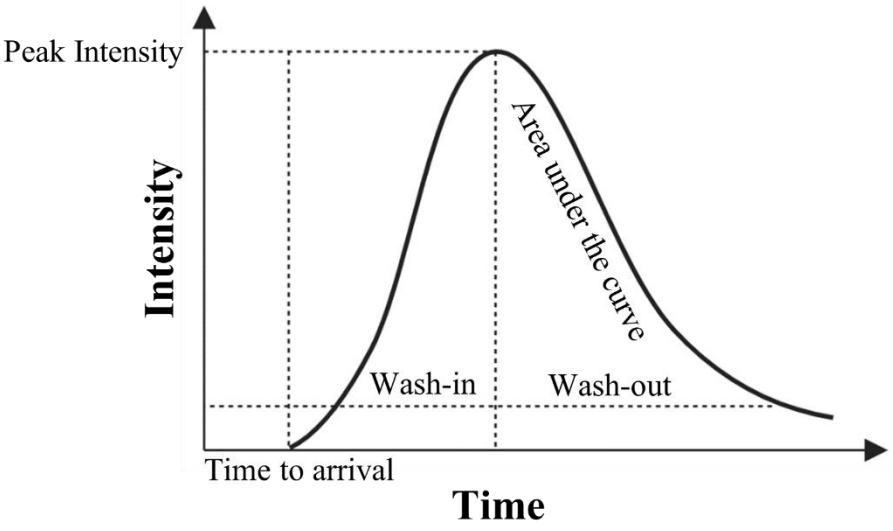

Figure 3. Example of a classic time intensity curve.

For DCE-US, ultrasound scattering microbubbles are used. Because of their size, microbubbles can pass through the smallest blood vessels. Furthermore, unlike tissue, they can reflect a non-linear ultrasound signal. An ultrasound wave can cause the microbubbles to compress at positive pressure and expand at negative pressure. This behaviour results in the reflection of an ultrasound signal containing the frequency of the driving wave, but also harmonic frequencies. These harmonic frequencies are a multiple or fraction of the driving frequency and can be filtered using a dedicated ultrasound sequence [23]. The main mechanism behind these non-linear imaging techniques is that they consist of multiple pulses, and when the response to the separated pulses is summed, the linear part of the signal is eliminated but the non-linear part remains. As a result, the microbubbles can be clearly followed through the vasculature by DCE-US.

Three of the most common compositions of non-linear sequences are called Pulse Inversion, Power modulation or Pulse Inversion Power Modulation, a combination of the previous two [23]. However, ultrasound manufacturers might give their non-linear imaging technique a different name, even if it is based on one of the common techniques. Moreover, the exact sequence and the used harmonics might not be specified [24].

2.2.2. Time intensity curves

DCE-US recordings offer visual information on the perfusion of the tissue. However, more quantitative information can be obtained when the pixel intensities are analysed over time and expressed in TICs. This section provides a detailed description of what TICs are and what kind of information they provide.

TICs are created by first selecting a ROI within the recorded plan, as shown in Figure 4. Next, the mean pixel intensity of all pixels in the ROI is plotted over time, resulting in a TIC, as previously shown in Figure 3. Analysation of TICs is based on underlying mathematical models. In general, when a microbubble bolus is injected, the TIC is considered to be the impulse response. From this impulse response, multiple parameters describing the hemodynamic can be derived. For example, the area under the curve is correlated to the local blood volume, while the wash-in time and wash-out time are related to the blood flow. On the other hand, the time to arrival provides little relevant information related to perfusion [12].

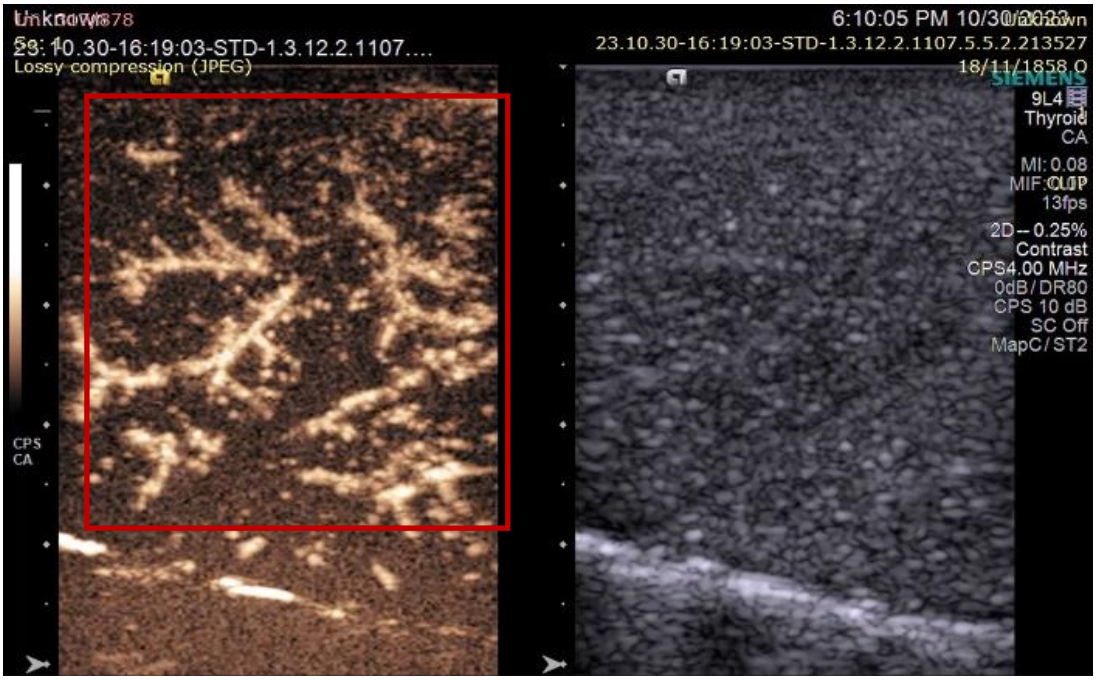

Figure 4. A screenshot of a DCE-US. Both the contrast-mode on the left and the B-mode on the right are shown. On the contrast-mode, a red ROI is selected to be analysed.

In the analyses of TICs, it is assumed that the microbubble concentration in the tissue is proportional [12]. Under this assumption, the Peak Intensity (PI) can be correlated to the microbubble dose in the ROI as a result of a bolus injection [25]. The PI is the intensity value at the exact moment in which the pixel enhancement, caused by the microbubbles, is at a maximum, see Figure Bb. As the PI is calculated from processed ultrasound data, it is often expressed in arbitrary units. The PIs from multiple measurements in the same ROI can be compared in order to determine in which instance the microbubble dose reaching the ROI was the highest. More specifically, the microbubble distribution in the ROI resulting from microbubble injections at varying catheter positions can be compared. However, the result has to be interpreted carefully, as the PI is given in arbitrary units which means it does not necessarily express the actual microbubble concentration. More in-depth information on this will be given in the next paragraph.

2.2.3. Microbubble quantification

Valuable parameters like the PI can be derived from TICs [12]. However, as the ultrasound signal recorded by the probe undergoes processing before it appears on the monitor, TICs present a modified signal. As a result of the data processing, the relation between the recorded signal and the PI is not straightforward [26]. Furthermore, it is assumed that the relation between the recorded signal and the microbubble concentration is linear [27]. In practise this assumption does not always hold [28]. In this section, it is described how a relation between the outcome of the TIC analyses and the microbubble concentration in the ROI can be recovered.

An overview of the chronological sequence from excited microbubbles to pixel intensity is given in Figure C. On the left side of the figure, it is indicated that microbubbles in the microvasculature are influenced by their environment and other bubbles. Further, the processing steps in the ultrasound machine from acoustic pressure to pixel intensity can be summarised as [25]: {3.} The output of the US transducer is a raw radio frequency (RF) signal, which is converted to a log-compressed signal quantised in gray-levels. {4.} The gray-level signal undergoes additional transformation to compensate for factors like the increasing attenuation with depth. {5.} Before the signal is displayed on the US monitor, a colour map is applied. The signal is hereby divided into a red, green and blue channel. {6.} For a clinical system like the Siemens Acusion S2000 (Siemens Healthineers, Erlangen, Germany) additional image enhancement options like Time Gain Compensation, Edge Enhancement and Custom Tissue Imaging could modify the signal even further [24].

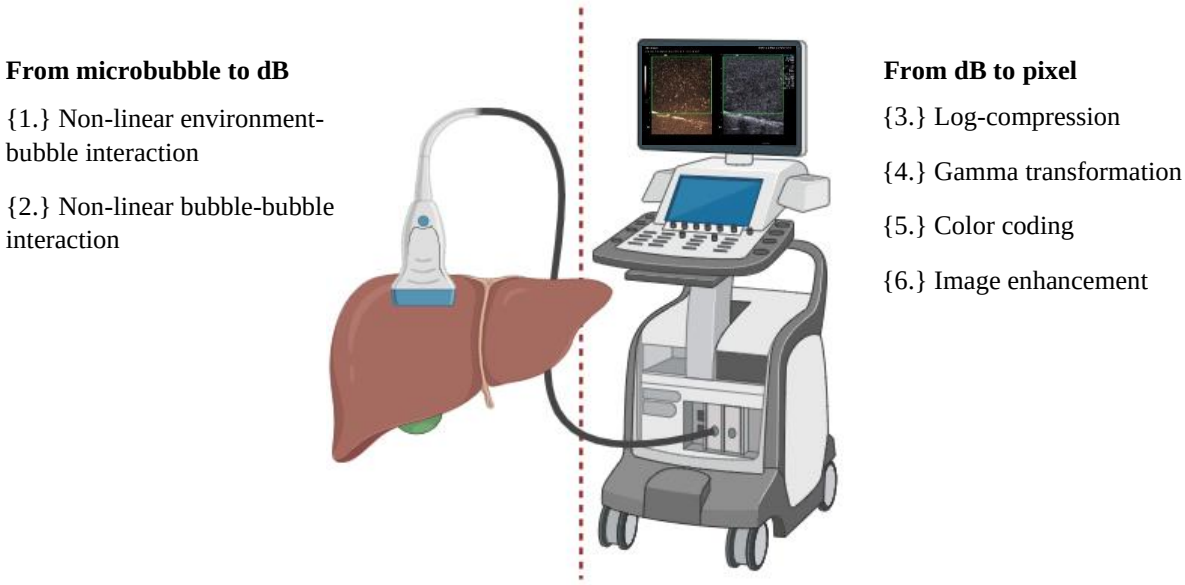

Figure 5. An overview of the signal pathway from microbubbles excited by ultrasound to pixel intensity. The left side summarises the steps taking place in in the tissue, and the right side shows the steps applied inside the ultrasound scanner.

To find the relation between PI and microbubble concentration, the first challenge is to reverse engineer the processing steps. If this is achieved, the raw RF signal could be retrieved from the processed data. Based on the raw RF data, the PI can be expressed in an acoustic pressure value in dB recorded by the probe. This would be one step closer to the real microbubble concentration. Reverse engineering would not be needed if the raw RF signal was made available by the US scanner. However, for most clinically used US scanners, this is not the case [26].

Two requirements for the retrieving of the raw RF signal from processed data are a sufficient dynamic range (DR) and adequate gain settings, this in order to prevent signal saturation or truncation [25]. If the reverse engineering is performed properly, the resulting quantification can be as accurate as when the raw RF signal were available [25].

The first measure would be to turn off all additional image enhancement options. Furthermore, there are general formulas to compensate for step {1} until {3} [25]. However, the variable values needed to solve the equations are not made available by the US scanners, as they are hidden or a rough generalisation of reality [12]. Therefore, reverse engineering with the available values would result only in a rough estimate, in which case the size of the possible error cannot be determined.

An alternative is the use of commercially available software with access to the necessary information. For example, VueBox (Bracco Suisse, Geneva, Switzerland) is a commercially available, ultrasound vendor independent quantification toolbox, which can analyse DCE-US DICOM clips, resulting in an estimate of the PI in dB.

VueBox is able to get access to the US scanner processing steps if it is equipped with a supplementary VueBox license. The necessary information will be passed on in a DICOM file as additional DICOM tags, see Figure 6. With this information, VueBox is able to produce an estimate of the PI that would be as good as could be

Module	Attribute	Tag	Type	Notes
VueBox	VueBox Header Info – Private Creator	(8FF1,0060)	3	Siemens Contrast Quantification
Contrast	Private Creator Version	(8FF1,6001)	3	1.0
Quantification	Log-compression dynamic range	(8FF1,6030)	3	Unit: dB VR = DS, VM = 1
Private	Total Gain	(8FF1,6031)	3	Overall contrast gain Unit: dB VR = DS, VM = 1
Attributes	Anti-log law vector	(8FF1,6032)	3	Inverse log-compression law for data linearization VR = DS, VM = 256
	TGC contrast gain vector	(8FF1,6034)	3	Will be present if transducer type is “LINEAR”, otherwise will be omitted. Unit: dB VR = DS, VM = 256
	Palette name	(8FF1,6035)	3	VR = LO, VM = 1
	Contrast Red Palette Data	(8FF1,6036)	3	Contrast palette RGB Values
	Contrast Green Palette Data	(8FF1,6037)	3	VR = IS, VM = 256
	Contrast Blue Palette Data	(8FF1,6038)	3	
	Transducer name	(8FF1,6040)	3	VR = LO, VM = 1
	Transducer frequency	(8FF1,6041)	3	Unit: MHz VR = DS, VM = 1
	Vector of destruction-frame numbers	(8FF1,6050)	3	VR = IS, VM = 1-n
	Number of destruction frames (n)	(8FF1,6051)	3	VR = IS, VM = 1
	Nonlinear Contrast Mode	(8FF1,6052)	3	VR = CS, VM = 1
	Allow Quantification	(8FF1,6053)	3	Set to “False” if gain, TGC, or dynamic range is changed during the course of the acquisition. “True” otherwise. VR = LO, VM = 1

Figure 6. A snapshot of the DICOM Conformance Statement of the ACUSION S Family Ultrasound System. It shows contents of the additional DICOM tags which are provided by the US scanner to Vuebox.

achieved even if raw RF data were to be used instead [26]. Again, the settings for the DR and gain during the DCE-US recording should be sufficient [27]. In combination with a Siemens Acusion S2000 (Siemens Healthineers, Erlangen, Germany), VueBox can analyse DCE-US clips in which the Contrast Pulse Sequence (CPS) is used. CPS is a combination of Power Modulation and Pulse Inversion and uses the fundamental and higher order harmonic signals generated by excited ultrasound contrast agents [29], [30] . A significant drawback is that the manuals of the ultrasound machine do not specify which sequence, or which higher order harmonics are used [24], [29].

With VueBox, analysing a US DICOM file containing a 45-seconds recording of a microbubble injection takes approximately three minutes. In order to do so, an ROI needs to be selected on the contrast-mode side of a dual-display, see Figure 7.

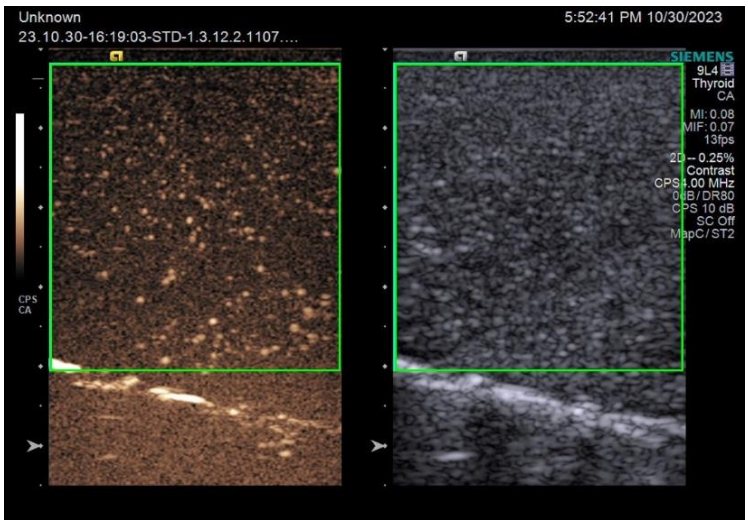

Figure 7. Example of a selected ROI in Vuebox. The green square is drawn by the user on the left side, the contrast-mode, and copied by Vuebox to the right side, the b-mode, for reference.

Vuebox will automatically mimic the ROI selection on the B-mode side for reference. Then, Vuebox will calculate a "preview" TIC in which the user needs to specify the moment of microbubble arrival, see Figure 8. Finally, VueBox produces a TIC fitted to the intensity data, from which an estimate of the backscattered acoustic PI can be derived in arbitrary and dB units. Unfortunately, VueBox cannot be used to perform real-time analysation of US recordings.

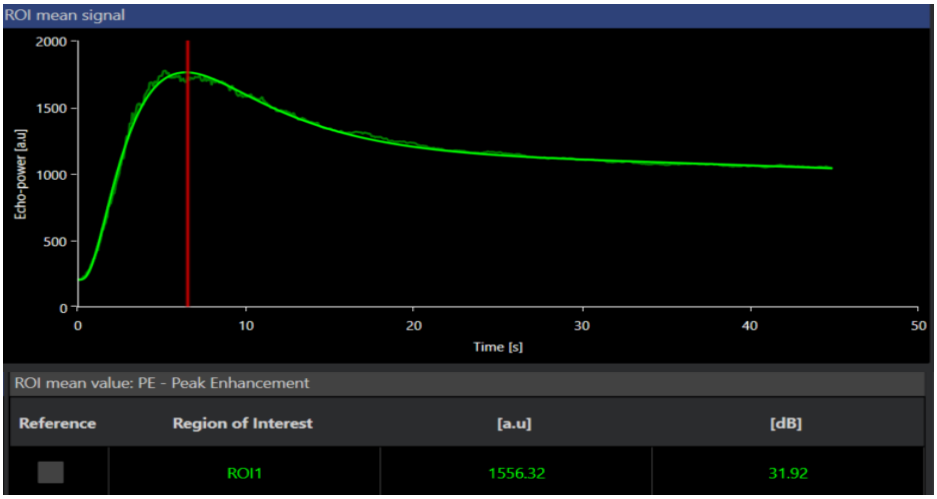

Figure 8. Example of a resulting TIC and PI output of Vuebox. A TIC if fitted by Vuebox over the intensity data from the point of microbubble arrival selected by the user. The resulting PI is given in an arbitrary unit, as well as in dB.

Now that we have found a way to derive a PI in dB, we will have a look into a way to establish the microbubble concentration. In literature, a constant proportionality model between the backscattered acoustic intensity and the microbubble concentration is described. This relation is proven to hold under certain conditions, which includes a microbubble concentration not exceeding 1 mL of diluted microbubbles per litre water, as is advised by the product manufacturer. Further, the microbubbles should be distributed homogenously [27], [31]. The relation can be written as follows

$$I(t) = \alpha C(t)$$

In the above equation, $I(t)$ denotes the backscattered acoustic intensity, $C(t)$ the microbubble concentration and α the describer of the relation, generally referred to as the backscatter coefficient [25]. Even with this model, absolute quantification remains impossible, as the value of α is unknown. When a baseline signal or noise β is introduced, the equation becomes

$$I(t) = aC(t) + ß$$

In theory, when the moment of microbubble arrival is selected in VueBox, the baseline signal is subtracted and the relation between $I(t)$ and $C(t)$ is proportional again. Then, the microbubble concentrations can be compared relatively, with a 3 dB difference indicating a doubling or halving of the microbubble concentration.

The microbubble concentration is the primary factor influencing the backscattered intensity [31]. Nevertheless, there are more influencing factors. Microbubbles give off the strongest signal when they are driven at their resonance frequency. Among other factors, the resonance frequency depends on the size of the microbubble, as can be seen in Figure 9. The smaller the bubble becomes, the higher its resonance frequency. Furthermore,

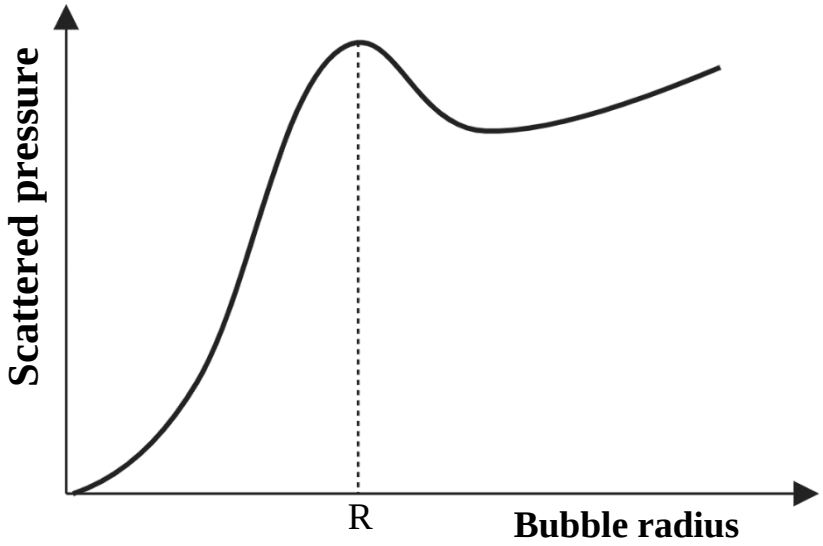

Figure A. The fundamental component of the response of microbubbles of increasing size on a fixed driving frequency. For the bubbles with size R, the driving frequency is the same as their resonance frequency. Therefore, they give off the most scattered pressure. For bubbles smaller than R the driving frequency is too low. For bubbles bigger than R, the driving frequency is too high, but they still generate a non-linear signal.

when microbubbles are used for DCE-US in practice, non-linear processes occur which are not represented by a linear model. For example, bubble dynamics are highly dependent on the biological environment and the presence of neighbouring bubbles.

Inside blood vessels, the blood vessel wall will reflect a part of the pressure field emitted by excited microbubbles. In turn, this has an effect on the microbubbles. For example, the elastic properties of the

surrounding wall influence the resonance frequency of the microbubbles. A more rigid wall causes a decrease, and a more elastic wall can cause an increase in resonance frequency. In extreme cases, the change of resonance frequency can be up to 40%. Another effect is that of the bubble-to-wall distance, which also has an influence on which frequencies are most dominantly emitted by the bubbles [28].

Assuming that during DCE-US a constant central frequency is emitted by the ultrasound probe, a change of the resonance frequency of the microbubbles results in a change of signal intensity, as radial oscillation of the microbubbles is bigger if they are excited at a frequency sufficiently close to their resonance frequency, see Figure A. Therefore, if a change in signal intensity is detected by DCE-US, it is unknown to which extent this is caused by a change in microbubble concentration or, for example, by a change in the bubble-to-wall distance.

Similarly, the presence of neighbouring bubbles influences the dynamics of a bubble by the sound field they generate [28]. The radial oscillation of a bubble is dependent on the inter-bubble distance [32]. The extent of this effect depends on the size difference between the bubbles. In an extreme case, this effect has shown to be able to cause a 10 dB difference in the signal output of a bubble [33]. For more details about microbubble behaviour, the review of Versluis et al. (2020) could serve as a good starting point [28].

2.2.7. Performing DCE-US

Considering the information provided in the previous paragraphs, the requirements of Vuebox and the limitations of microbubble concentration models, the subsequent recommendations for the settings have been established.

- Dual-display modus of the B-modus and contrast-modus should be activated, in order for Vuebox to work [34]. Besides, some structures are better distinguishable on the B-modus screen [12].

- The frequency is chosen as a compromise between microbubble response and resolution, as the resonance frequency of most clinical used microbubbles is around 1-2 MHz [12].

- A frame rate between 8 and 15 Hz is advised by VueBox [34].

- The acoustic power expressed in mechanical index (MI) should be below 0.1 in order to prevent bubble destruction. However, as different manufacturers measure the MI with different methods, caution is needed. To test the MI settings, when switching to a new plain, no microbubble destruction (a sudden decrease in intensity) should be observed [12].

- The DR should be greater than 40 dB, which is required for accurate reverse engineering of the PI in dB. However, the DR shown by the US system is often not the actual one. Therefore, it is advised to use an even higher value. This might cause the images to look “dull” with a low variation of grey, but it is the better option for DCE-US [12].

- The gain should be chosen in a way that prevents signal saturation, but is also high enough to enable detection of low amplitude microbubble signals, as the MI is set fairly low [12].

- The time gain compensation should be set at a central position for a “fair” quantification [12].

- The focus should be placed to be at least at 2/3 of the ROI, but preferably lower than the ROI, for the most homogenic acoustic field. This will lead to the most uniform excitation of the microbubble in the image plane [12].

- The depth needs to be slightly longer than the depth needed to visualise the whole ROI, in order to ensure the focus can be placed below the ROI [12].

- The clip length should be sufficient to measure the wash-in and start of the wash-out if the peak intensity (PI) is of interest [34].

- The pulsing scheme should be non-linear. On the Siemens Acusion S2000 two pulsing schemes are available: Contrast Pulse Sequencing (CPS) and Contrast Harmonic Imaging. There is no detailed explanation on the schemes present in the user manuals [24]. In order to use VueBox, CPS is required [34].

- The space time option is a trade-off between image line density and frame rate [24]. As long as the lower frame rate limit of 8 Hz can be reached, the image line density should be prioritised in order to uniformly excite the microbubbles in the image plane.

- The persistence should be turned off in order to avoid averaging of the image data between consecutive frames, as this could smooth out the PI [22].

- The chosen colour map should be compatible with VueBox [34].

- The chosen tint should also be compatible with Vuebox [34].

- Additional image enhancing settings such as Tissue Harmonic Imaging, Edge Enhancement, Custom Tissue Imaging, etc., should be turned off, as their influence is unknown and therefore impossible to compensate for.

- The selected ROI should not contain large vessels if the parenchyma is of interest and the other way around, as the moment of microbubble arrival is not the same. Therefore, an ROI including both would result in a TIC that provides only a general overview of the in- and outflow times of microbubbles in the tissue and parameters as the PI would then be less valuable.

- In order to limit the non-linear behaviour of a bolus of microbubbles, a concentration of up to 0.1 mL of diluted microbubbles per 100 mL water should be used.

- Furthermore, in an attempt to level out the effect of size differences of the bubbles between multiple measurements, the mixture of microbubbles should be rotated prior to injection. Doing this will ensure a more homogenous size distribution.

Chapter 3 | Real-time analysis of Dynamic Contrast Enhanced Ultrasound for catheter position optimisation in Transarterial Radioembolization: a proof-of-concept study in an ex-vivo perfused porcine model

A. Visser[1], J.L. van der Hoek[1], T.J. Snoeijink[1,5], M.E. Krommendijk[1], H.R. Liefers[2], J.G.M. Greve[2], M. Versluis[3], J. Arens[4], S. Manohar[1], E. Groot Jebbink[1]

1. Multi-Modality Medical Imaging group, University of Twente, Enschede, The Netherlands
2. TechMed Simulation Center, University of Twente, Enschede, The Netherlands
3. Physics of Fluids group, University of Twente, Enschede, The Netherlands
4. Engineering Organ Support Technologies group, University of Twente, Enschede, The Netherlands
5. Department of Medical Imaging, Radboud University Medical Centre, Nijmegen, The Netherlands

Email: a.visser-3@student.utwente.nl

Abstract Transarterial Radioembolisation is a treatment option for unresectable liver tumours. In this treatment, a microcatheter is guided towards the hepatic arteries supplying the tumour, to selectively inject radioactive microspheres which embolise the capillaries and locally irradiate the tissue. However, the absence of real-time visualisation of the microsphere deposition during the treatment can lead to sub-optimal targeting of the tumour and unpredicted off-side toxicity. As the effectiveness of the treatment is related to the tumour absorbed dose, the microsphere deposition at the tumour location should be optimised. We present here for the first time an augmented Transarterial Radioembolisation protocol using a combination of microbubbles and real-time quantification of Dynamic Contrast Enhanced Ultrasound data to provide visual feedback during the treatment. For this purpose, an in-house algorithm with the capacity to instantly generate and quantify Time Intensity Curves was developed. In a carefully controlled laboratory setting, using an ex-vivo perfused porcine liver, we demonstrate that the live feedback of our novel approach enabled efficient optimisation of the catheter position such that a predefined area is targeted.

I. Introduction

In this proof-of-concept paper, an augmented protocol for the Transarterial Radioembolisation (TARE) procedure is proposed. TARE is a palliative treatment option for unresectable hepatic tumours performed over 20.000 times each year, worldwide [4]. The goal of the treatment is to selectively target the tumour with a high dose of radiation, while preserving the healthy parenchyma. Through an arterial-inserted microcatheter, arteries supplying the tumour are targeted with microspheres filled with a radioactive isotope: yttrium-90 (^{90}Y) or holmium-166 (^{166}Ho). The microspheres embolise the capillaries downstream, blocking the blood flow to the tumour and locally target the tissue with a high radiation dose [15].

The overall survival of TARE improves with a higher tumour radiation-absorbed dose [7]. Therefore, the microsphere deposition at the tumour location should be optimised [7]. However, a considerable limitation of the current approach is the lack of real-time visualisation of the microsphere during the treatment. Currently, the microsphere distribution resulting from the injections can only be assessed afterward by Magnetic Resonance Imaging (MRI) or

Single Photon Emission Computed Tomography (SPECT) in combination with CT. The absence of real-time feedback during the treatment leads to suboptimal results and risk of unpredicted off-side toxicity [10]. Current strategies to control the microsphere deposition depend on the microsphere distribution results of a pre-treatment treatment-mimicking scout injection of holmium-166 (^{166}Ho) or technetium-99m macroaggregated albumin (^{99m}TC-MMA). However, the utility of this treatment-mimicking injection is compromised by changes in hemodynamic conditions, variations in injection velocity and challenges in reproducing the injection site during the final treatment [8]. Numerical simulations have shown that the catheter position has a great influence on the microsphere distribution, with a difference up to 40% by an axial position variation of merely 5 mm [9]. For better control over the microsphere distribution, we propose an augmented protocol for the TARE procedure with real-time feedback.

As microbubbles follow the same trajectories as ^{166}Ho microspheres [11], it is hypothesised that microbubbles can be used to determine the most optimal catheter position. With Dynamic Contrast Enhanced ultrasound (DCE-US), microbubble presence in tissue can be visualised and quantified using time intensity curves (TICs) [12]. Furthermore, based on real-time analysis of the TICs, the results of microbubble injections at various locations can be compared. In this way, the catheter position resulting in the highest number of microbubbles in the target region can be determined. Ultimately, this could result in an optimised tumour radiation-absorbed dose, while preventing off-side toxicity. The protocol will be tested by targeting an arbitrarily selected location on an ex-vivo perfused porcine liver, which closely resemble a human liver [35].

II. Methods

Liver preparation

Porcine livers were procured at a slaughterhouse (Vion Groenlo B.V., Groenlo, Netherlands). The liver was prepared according to our in-house protocol, included in Appendix A. In summary, within 30 minutes after receiving the organ, the liver was flushed with 3L cold saline solution with 25000 units of heparin through the portal vein cannula. In the following 4 hours, the hepatic artery was dissected until the level of the aorta. All branches not supplying the liver were ligated and the aorta was cannulated.

Ex-vivo setup

A schematic overview of the setup is shown in Figure 1. The liver was perfused normothermic (37°C) with 5L of porcine blood mixed with 6 mL/L saline solution, 1.8 ml/L 50% glucose and 15000 units of heparin to prevent blood clotting. The complete perfusion protocol is presented in Appendix A. For the arterial circulation, the perfusate from the reservoir was pumped to the liver by a Xenios NovaLung iLA ACTIVVE (Xenios AG, Stolberg, Germany) pump. On the venous, side the flow was driven by a Maquet Rotaflow (Maquet, Rastatt, Germany) pump. Two oxygenators, a PLS-i (Maquet, Rastatt, Germany) on the arterial side and a Hilite 800 LT (Medos Me AG, Stolberg, Germany) on the venous side, provided the heat exchange which was regulated by a Hico Veriotherm 550 (Hico Medical Systems, Köln, Germany) heat exchanger. Additionally, the oxygenator on the atrial side also

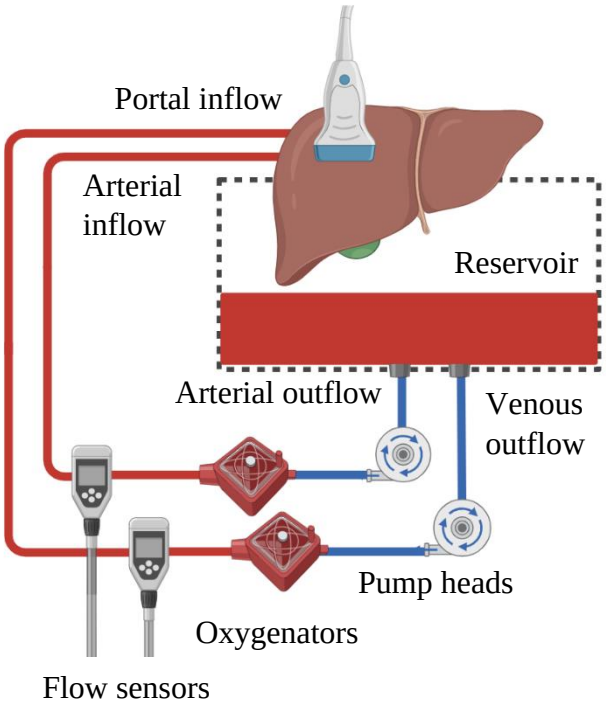

Figure 1. Overview of the ex-vivo set up. Not shown are the: heat exchangers to the oxygenators, oxygen supply to the arterial oxygenator and pump consoles controlling the pump heads. More details about the positioning of and connection to the liver are shown in Figure 2.

supplied oxygen. The flow was measured both on the arterial and venous side with Sonoflow CO.55 V2.0/140 (Sonotec, Halle, Germany) flow sensors. The liver was suspended above the reservoir on a perforated mat, to let the perfusate drain from the liver, see Figure 2.

Microbubbles

BR-14 microbubbles (Bracco Suisse, Geneva, Switzerland) were used as contrast agents. For every measurement, a 1:5 diluted bolus of 0.2 mL was injected during 5 seconds, followed by a 10-second flush of 5 mL phosphate buffered saline solution. A haemostatic valve was installed just upstream of the arterial cannula to allow insertion of a microcatheter, see Figure 2. The catheter was connected to a syringe injection pump (SyringeTWO, New Era Instruments, New York, United States) to perform a controlled injection of microbubbles, together with an additional injection pump (PHD ULTRA, Harvard Apparatus, Holliston, United States) which could provide the flush. In order to homogeneously suspend the microbubbles, the 3 mL syringe was continually rotated by a prototype rotation device (Quirem Medical B.V., Deventer, The Netherlands). Filtering of the microbubbles from the recirculating perfusate, to prevent a second pass through the liver, was facilitated by the oxygenators together with the Xenios and Maquet Rotaflow pumps.

Figure 2. Liver above the reservoir on a perforated mat. The blue canula connects the portal vein and de orange cannula the hepatic artery. Furthermore, the ultrasound probe placed on of the lobes is visible.

DCE-US

To perform the DCE-US measurement, a target location at one of the liver lobes was selected for the placement of a 9L4 linear transducer (Siemens Acuson S2000, Siemens Healthineers, Erlangen, Germany). The position was designated based on the absence of major vessels on B-mode images, as the parenchyma was of interest [18]. Moreover, a smooth surface without scarring was selected, in order to keep the eventual hampering of the acoustic transmission to a minimum. For the acquisition, a Siemens proprietary non-linear pulsing scheme called Contrast Pulse Sequencing was used [30]. The transmitted frequency was 4 MHz and the frame rate was capped at 13 Hz.

With an imaging depth of 5.5 cm, the full cross-section of the lobe was visualised. To provide a homogeneous acoustic field, the focus was set as low as possible, resulting in a depth of 5.0 cm. The standard amplitude of the ultrasound pulse was turned down to 0.25%, resulting in a mechanical index (MI) of 0.08, to prevent bubbles from collapsing [12].

In-House Algorithm

The real-time feature of the protocol was provided by an in-house developed MATLAB (R2023b; The MathWorks, Natick, MA, USA) algorithm. The DCE-US video data, visible on the monitor of the ultrasound machine, was live streamed to the algorithm, through a HDMI cable and via a frame grabber (HDMI Capture Card, Edco Goods, Eindhoven, The Netherlands). Upon clicking the "run" button, the algorithm records the streamed video data for 45 seconds, which is sufficiently long to capture a complete microbubble injection. At the end of the first measurement, the algorithm asks to select an ROI on the first recorded frame, which is then subsequently applied to all successive frames and measurements. Next, the algorithm calculates the mean pixel intensity of the ROI over the duration of the measurement and visualises this in a TIC, see Figure 3.

Analysation of TICs is based on underlying mathematical models. In general, when a microbubble bolus is injected, the TIC is considered to be the impulse response. From this impulse response, multiple parameters describing the

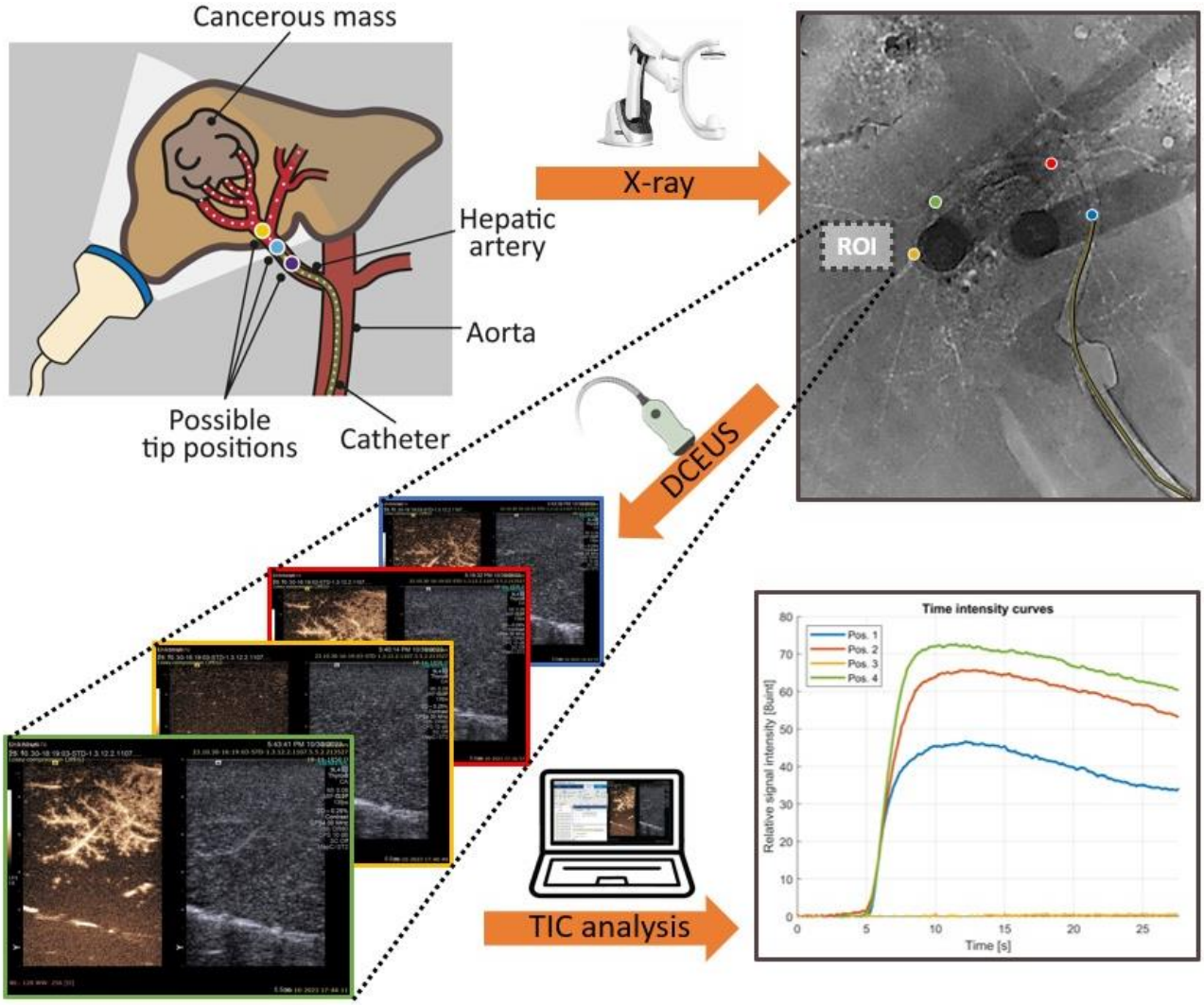

Figure 3. Iterative workflow overview.

hemodynamics can be derived. For our purposes, the focused is on the peak intensity (PI). The PI is the intensity value at the exact moment in which the pixel enhancement, caused by the microbubbles, is at a maximum. As the PI is calculated from processed ultrasound data, it is often expressed in arbitrary units [12]. The PIs from multiple injections at varying catheter positions can be compared, in order to determine which catheter position resulted in the most microbubbles reaching the ROI. To ease PI comparison of multiple measurements, the elapsed time between the microbubble injection and the first appearance of microbubbles in the ROI is normalised.

Microbubble quantification

To give the user more direct information about the microbubble concentration instead of the pixel intensities, the TICs are converted to dB. Since the raw US channel data were not available and the signal processing steps of the US machine were unknown, an in-house *translation factor* between the pixel intensities and microbubble concentration was formulated. In previous microbubble measurements in ex-vivo perfused pig livers, the US monitor pixel intensities were compared to the dB output of commercially available quantification software VueBox (Bracco Suisse, Geneva, Switzerland). Based on these measurements, a linear fit between the pixel values in 8-bit and microbubble concentration in dB was calculated, which gives an estimate of the microbubble concentration. Hereby, a 3 dB difference suggests a doubling of the concentration. For a detailed description of the *translation factor*, see Appendix C. After the experiment, our estimated real-time results are compared with non-real-time results of VueBox.

Furthermore, in order to compensate for the lack of raw data, it is crucial to prevent signal saturation or truncation [26]. Recovering the true dB values based on clipped data is impossible, which hampers the estimation of the microbubble concentration. To prevent this, a sufficient dynamic range (DR) and gain setting should be chosen [36]. For this purpose, the algorithm includes a *Gain & Dynamic Range Check*, developed based on previous in-vitro measurements. For more details, see Appendix D. After the user has selected an ROI on the DCE-US frame, the algorithm automatically plots a histogram of the pixel distribution of the brightest frame. If the range of pixel values fits on the 8-bit grayscale, the gain and DR settings are sufficient. Based on the *Gain & Dynamic Range Check* the DR was set to 80 dB and the gain to 10 dB. Additional signal adjusting settings were turned off or limited as much as possible. In this way, the reverse calculated dB values would be the most accurate [12].

Real-time catheter position optimalisation

In order to find the catheter position from which the highest number of microbubbles reach the ROI, injections at multiple locations were analysed. The microcatheter was maneuvered into position using digital subtraction angiography of the hepatic arterial tree (ARTIS Pheno, Siemens Healthineers, Erlangen, Germany). After positioning the catheter, a bolus of microbubbles was injected just before the algorithm was started. A successive catheter position was determined based on the PIs from the TICs combined with artery maps from the angiogram. At each location, the measurement was repeated 3 times. Prior to each measurement, A high MI pulse called Burst, lasting 10 frames, was applied in order to destroy the remaining microbubbles in the ROI.

Holmium-165 microsphere deposition assessment

After the optimal position was determined, an injection of 300 mg non-irradiated holmium-165 microspheres (^{165}Ho-MS) (Quirem Medical B.V., Deventer, The Netherlands) was performed, followed by a 25 mL saline flush to rinse all remaining microspheres from the catheter. To assess the ^{165}Ho-MS deposition, a T_2^* multi-gradient MR scan was performed 15 hours after the experiment.

III. Results

The liver was prepared according to the in-house protocol, keeping the warm ischemia time below 30 minutes. During the perfusing, the arterial and venous flows were 900 ml/min and 300 ml/min respectively. The temperature of the perfusate was regulated at 37˚C and the oxygen supply was set to 500 ml/min, delivered solely to the arterial oxygenator.

The DCEUS tracking of the microbubbles down to the capillary level is shown in Figure 4. In Figure 4d, it is shown that the microbubbles did not extend fully to the lower edge of the liver, indicated by the blue arrows.

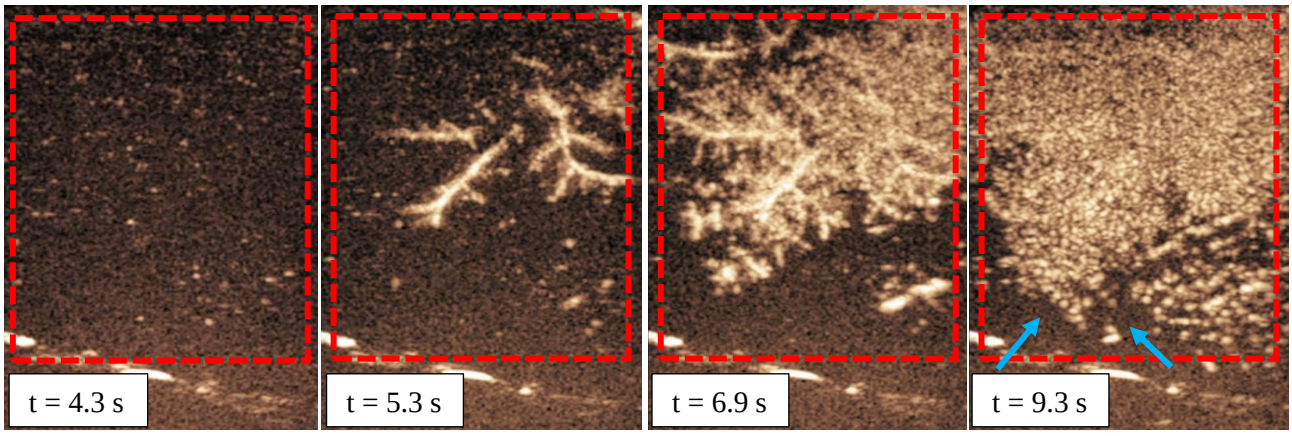

a. **b.** **c.** **d.**

Figure 4. DCE-US images of a microbubble injection at catheter location P4. Time after injection is indicated in each subfigure. The diagonal line present in all four images is lower edge of the liver. The red squares specify the ROI used for analysis. The blue arrows point to areas which the microbubbles did not reach **a.** Moment before the microbubbles arrive. **b.** Microbubbles entering the arteries. **c.** Microbubbles spread to smaller vessels. **d.** Moment of peak intensity, the microbubbles have spread through the parenchyma.

The in-house developed algorithm generated real-time TICs of the microbubble injections, based on the video data of the ROI indicated in Figure 4. The PIs of the multiple locations provided immediate feedback on the influence of the catheter positioning. Figure 5 shows TICs of the 4 positions together with their corresponding location on the angiogram. The first position is indicated with P1, after which the catheter was located a bit further back, in the more common left hepatic artery at P2, and thereafter more specifically at P3. Based on the relation between the catheter position and the resulting PIs, the main supplying artery branch of the ROI could be identified. More specifically, because of the dropped

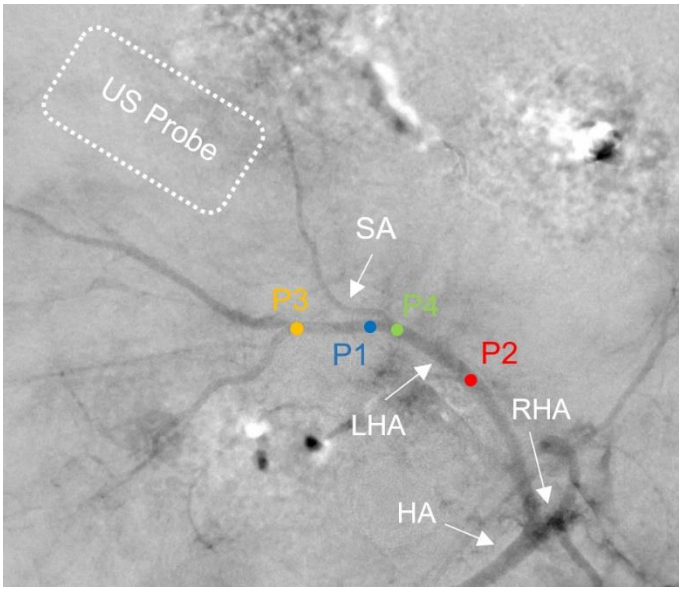

a.

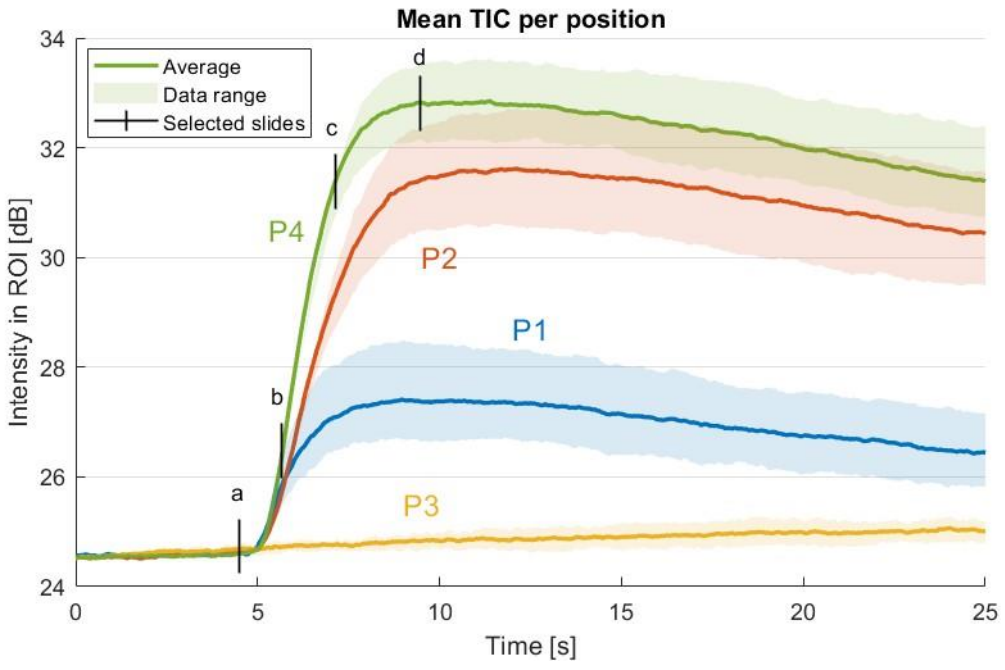

b.

Figure 5. **a.** One of the angiograms. The different catheter positions are indicated by the colored dots. The hepatic artery (HA), left hepatic artery (LHA), right hepatic artery (RHA) and the main supplying artery (SA) are pointed out by white arrows. The location of the US probe is shown by the dotted square. **b.** The injection-time normalized averaged TICs of 4 catheter positions. The numbering of the graphs correspond with the chronologic order in which the measurements were performed. The solid line shows the average of the 3 injections per position and the shaded areas visualizing the minimal and maximal values. The black vertical lines correspond with the images showed in Figure 5.

PI at P3, it was known that the branching of the supplying artery was located back. At P4 the catheter was positioned in front of the supplying artery, where the microbubble injection and analysis resulted in the highest PI. Subsequently, an injection of 300 mg ^{1650}Ho microspheres at this position was performed.

Table 1 shows the estimated microbubble concentration resulting from the translation of the PI values from 8-bit to dB. For validation, the non-real-time dB values found by VueBox are also shown, excluding P3. Here, VueBox produced no results due to the absence of the typical wash-in and wash-out pattern in the TICs.

Figure 6 shows the deposition of the ^{165}Ho microspheres indicated by the black dotted pattern on a T_2^* multi-gradient MR scan, performed 15 hours after the injection. ^{165}Ho microspheres are present in the target lobe and an adjacent lobe, which is also perfused by the left hepatic artery. Additionally, indicated by the yellow arrow, rings caused by the supporting mat were visible at the bottom of the liver.

Tabel 1. Comparison of PI results per measurement

Position	Nr.	PI [dB] MATLAB	PI [dB] VueBox	Difference [dB]
1	**1**	26.76	26.44	-0.29
	2	27.00	26.89	-0.09
	3	28.65	29.09	0.45
	Mean	**27.47**	**27.47**	**0.00**
2	**1**	31.29	33.25	1.98
	2	30.65	32.52	1.89
	3	32.69	34.32	1.65
	Mean	**31.54**	**33.36**	**1.82**
3	**1**	24.84	-	-
	2	25.28	-	-
	3	25.10	-	-
	Mean	**25.07**	-	-
4	**1**	31.99	33.35	1.38
	2	33.34	35.34	2.02
	3	32.47	34.26	1.81
	Mean	**32.60**	**34.32**	**1.72**

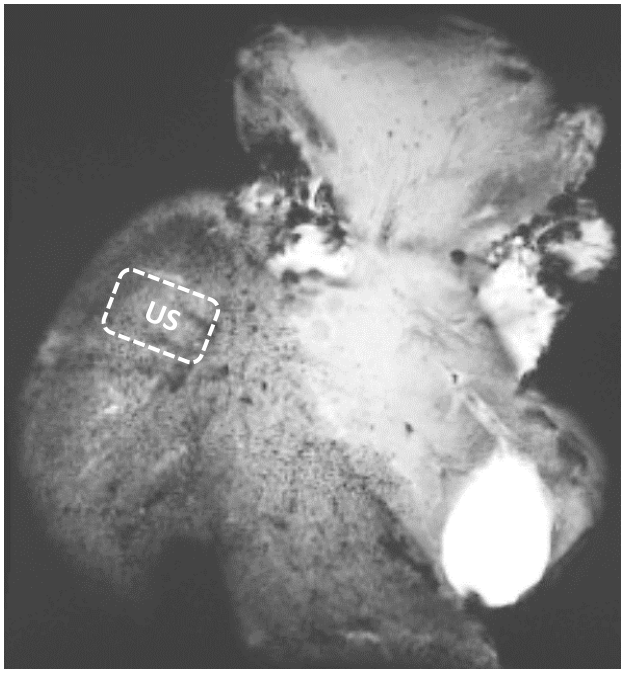

Figure 6. One slide of the a T2*multi-gradient MR scan performed after holmium injection a P4. The position of the ultrasound probe is indicated by the dotted square.

IV. Discussion

In this ex-vivo feasibility study of a DCE-US guided TARE protocol, it is demonstrated for the first time that the catheter position can be optimised based on quantitative real-time TIC analysis of DCE-US imaging in a perfused porcine liver. DCE-US was successfully performed on a perfused porcine liver, as shown in Figure 4. The in-house developed algorithm provided adequate real-time feedback on the catheter position, shown in Figure 5. Based on the PI of multiple microbubble injections, the optimal catheter position for targeting the predefined ROI could be determined. After converting grayscale values to dB, the improvement compared to the other considered positions ranged from 25% to 330%. The post treatment T_2^* MR image in Figure 6 shows that ^{165}Ho-MS reached the target region after injection at a location chosen based on the microbubble distribution.

Algorithm

To the best of the author's knowledge, no previous studies have used real-time DCE-US analyses to optimise the catheter position for targeting a predefined ROI. In this paper, it is demonstrated how the in-house developed algorithm provided real-time feedback on the catheter position during an ex-vivo

simulated TARE procedure. As DCE-US recordings are translated to TICs expressing the estimated microbubble concentration in dB, the user gains insight in which position would lead to the highest holmium concentration in the ROI, as it is assumed that the holmium microspheres follow the same trajectory as the microbubbles [11]. These results suggest that a DCE-US guided TARE protocol may help optimise the treatment, as TARE is more effective if the dose received by the tumour is higher. Furthermore, the *Gain & Dynamic Range Check* of the algorithm assists the user in choosing the optimal settings for DCE-US, given the ROI and possibilities within the clinical environment of the US scanner. Additionally, the algorithm is vendor independent as it requires US display data through a HDMI output.

Quantifying uncertainty

It is important to bear in mind the uncertainty that comes with the output of the algorithm. Like other quantitative DCE-US analysing tools, the provided microbubble concentration is always an estimation based on several assumptions [26]. The backscattered ultrasound intensity of an injected polydisperse microbubble bolus is influenced by unknown variables like the size distribution, inter-bubble distance and elasticity of the surrounding blood vessel wall [32], [37]. Because of these uncertainties, the true concentration cannot be determined. In future research, monodisperse bubbles could be used in order to reduce the uncertainty, for their behaviour is more predictable [32]. Nevertheless, given that the concentration is the primary factor influencing backscattered intensity, it is still possible to give an meaningful estimation [31]. If the algorithm proves to provide relevant information, it can be a useful addition to the current practice. In this feasibility study, it is shown that, based on the feedback from the algorithm, a catheter position targeting the ROI could be selected, as confirmed by the T_2^* MR scan.

A second aspect that contributes to the uncertainty is the lack of disclosure regarding the signal processing steps from backscattered intensity to pixel values. Therefore, the true *translation factor* is unknown to a clinical mode DCE-US user. This could have contributed to the difference between the in-house algorithm and VueBox, which has access to this information [26]. At the three positions a difference of 0.0 dB, 1.82 dB and 1.72 dB between the analysing strategies was measured. Regardless of these discrepancies, the two approaches are in agreement on which catheter positions resulted in the highest and lowest microbubble concentration in the ROI. Additionally, between P2 and P4 a difference of 1.06 and 0.96 Bb is shown by the *translation factor* and Vuebox respectively. This indicates a 25% difference in microbubble concentration between the locations. On the difference between P1 and P4 the *translation factor* reports a 5.13 dB change and VueBox states a 6.85 dB increase from P1 to P4. This represents a concentration which is 330% and 440% higher. The quality of quantification could be improved if US manufacturers were to provide the assumptions the system works with, as suggested by Turco et al. (2020). Meanwhile, future work is needed to generate additional data, allowing for a more precise estimation of the *translation factor*.

Comparison to other work

In previous studies on the improvement of TARE, alternative strategies to provide more feedback during the treatment are explored. Several approaches are based on applications of CT. The overall advantage of CT over US is the larger field-of-view. This could result in a more complete overview of the effects of the treatment, extended to other organs outside the liver. O'Conner et al. (2020) proposed an alternative method to evaluate the work-up procedure with an intra-treatment cone-beam CT, allowing for more accurate pre-treatment dosimetry [38]. However, Martin et al (2021) found that cone-beam CT does not significantly increase the accuracy of treatment dose prediction compared to the existing strategy [39]. A possible explanation for this might be the remaining challenges in reproducing the catheter position in the final treatment [8].

Taiji et al. (2023) presented a novel approach which could potentially overcome this issue by combining the work-up and final treatment into one section [40]. With the proposed method, the feeding arteries to the tumour can be identified based on intra-treatment CT hepatic arteriography enhancement mapping, Subsequently, the embolising particles are injected. Feedback on the injection is provided by additional CT hepatic arteriography, on which the closing of the tumour feeding arteries is visible. A limitation of this

approach is the absence of direct feedback on the particle distribution. As feedback is only provided after the injection, the possibility to optimise the catheter position is limited. An additional drawback is that the potential flow of the embolising particles to the tumour is estimated based on the distribution of CT contrast agent. This distribution is not necessarily a reliable predictor of the particle trajectory, especially when the injection is close to a bifurcation [41].

Dietze et al. (2023) developed a hybrid SPECT and cone-beam CT scanner for an augmented TARE protocol which merges the work-up and final treatment and allows for feedback on the catheter position based on ^{99m}Tc-MMA scout injections [42], [43]. However, the studies on the new scanner published so far do not assess the usability of the produced cone-beam CT/SPECT images for catheter optimalisation [44]. Besides, both the hardware and software require further improvement in terms of image quality [45], and analysation speed [44], before the scanner is suitable for clinical use [42].

Our protocol addresses all of these drawbacks. First of all, it is based on an established ultrasound technique. Additionally, the required ultrasound scanner might already be present in the intervention room for the insertion of the microcatheter into the femoral artery [16]. Moreover, in this work it is shown that the required analysis can be performed real-time. Furthermore, a randomised pilot control trial by Eisenbrey et al. (2021) showed the potential for an improved treatment response by combining TARE with US-triggered microbubble destruction [46]. Our catheter position optimising protocol involving microbubbles might seamlessly combine with such microbubble-based therapies.

Limitations

In this study, the ex-vivo perfused porcine liver served as a controllable, detailed and dynamic model [35]. Figure 4 shows how, at the moment of peak enhancement, the microbubbles have spread through the parenchyma. Yet, the lower region remains relatively dark. This is also visible in the results of the ex-vivo perfused porcine liver microbubble experiments of Izamis et all. (2014), who mention a "generally homogeneous" distribution [22]. These results seem to indicate a limited perfusion in this region, because microbubbles cannot enter when vessels are closed off. This might be a result of insufficient perfusion settings. Another possible explanation is that the vessels in this region are closed off by excessive pressure from the weight of the liver itself against the supporting mat, as marks of the rings of the mat were visible in the tissue on the MRI. As this might have an influence on the analyses of the ROI, further investigations are required to gain a better understanding of the possible cause of the dark lower region. The particle distributions in DCE-US with a higher microbubble concentration or quantitative T_2^* multi-gradient MR might lead to clearer visualisation of what is happening in the tissue. Additionally, blood sample tests might give more information about the viability of the tissue.

The augmented procedure described in this study allows for real-time feedback on the microsphere distribution, and therefore optimalisation of the catheter position. However, the results of the experiments do not display the full potential of the proposed procedure. The post-treatment T_2^* multi-gradient MR scan showed a microsphere deposition outside the target area in a smaller adjacent lobe. Due to time constraints, only 4 positions were examined during the measurements. Further optimalisation of the catheter position could possibly have led to a holmium deposition limited to the target area. The two main improvable time-consuming factors were the restrictions of the hybrid OR on radiation exposure to the researchers, and the low visibility of the catheter on the angiograms. Currently, the OR had to be unmanned for the use of radiation, hampering the workflow. Additionally, it is recommended that in future research the injection of contrast fluids is performed through the catheter tip, which causes the tip to be easier identifiable on the angiogram.

In spite of its limitations, the results of this study do provide insights into the feasibility of the alternative protocol, and ex-vivo experience on the importance of the catheter position was gained. Additionally, it provides us new information on where the biggest challenges of the whole procedure might lie, and which aspects to focus on in further research.

V. Conclusion

We present here for the first time an augmented TARE protocol using a combination of microbubbles and real-time quantification of US data to optimise the catheter position for subsequent administration of holmium microspheres. For this purpose, an in-house algorithm with the capacity to instantly generate and quantify TICs was developed. In a carefully controlled laboratory setting, using an ex-vivo perfused porcine liver, we demonstrate that the live feedback of our novel approach enabled efficient optimisation of the catheter position such that a predefined area is targeted.

Appendix A | Summary of the porcine liver preparation and perfusion protocol

A.1 The procuring and preparation of a porcine liver

The preparation of a porcine liver for perfusion takes roughly 3 hours, excluded transport time if the liver is procured at a slaughterhouse. This paragraph provides a chronological summary of the necessary liver preparation steps which needs to be performed in the slaughterhouse and experiment location [47].

At the slaughterhouse

When an organ package is obtained at the slaughterhouse, the goal is to be ready for transport in 30 minutes, as the warm ischemia time should be limited to 30 minutes for a viable liver. Since the warm ischemia time is of critical importance, the liver should be flushed with cold saline as fast as possible. Therefore, the first step is to dissect the portal vein so it can be cannulated, after the liver is inspected for any signs of damage and the heart and lungs are removed to make the package more workable. Once the hepatic vein is cannulated, the liver is flushed with 3L cold saline, with the first litre containing heparin to prevent coagulation. It is a good sign in terms of time management if this flush is provided within 15 minutes. The next step is to remove the remaining organs and to tie off the cystic duct leading to the gall bladder. After the liver is completely cut out of the total organ package, it should be placed in a plastic bag and flushed with another 0.5L of saline. For transport, the bag containing the liver and the saline is placed in a cooler box with ice. This is considered as the end of the warm ischemia time and start of the cold ischemia time.

At the experiment location

The remaining preparation steps before the liver can be connected to the perfusion machine are performed at the experiment's location. The first step is to dissect the hepatic artery at the level of the aorta. All branches not supplying the liver needs to be ligated. Because of anatomical variances, the number and location of this branches is hard to predict beforehand. If this is done successfully, the aorta before the hepatic artery branch is canulated and the part after is tied off. Completion may take up to 2.5 hours. This however is not a problem since the cold ischemia time has a less drastic influence on the liver viability than the warm ischemia time.

An image of a completely prepared porcine liver is shown in Figure 1. The liver might appear 'greyish' because of the absence of blood, which is removed during the flush. Further, on top of the aorta the black surgical suture thread is visible. With this suture, the cannulas are secured and all excessive vessels are tied of.

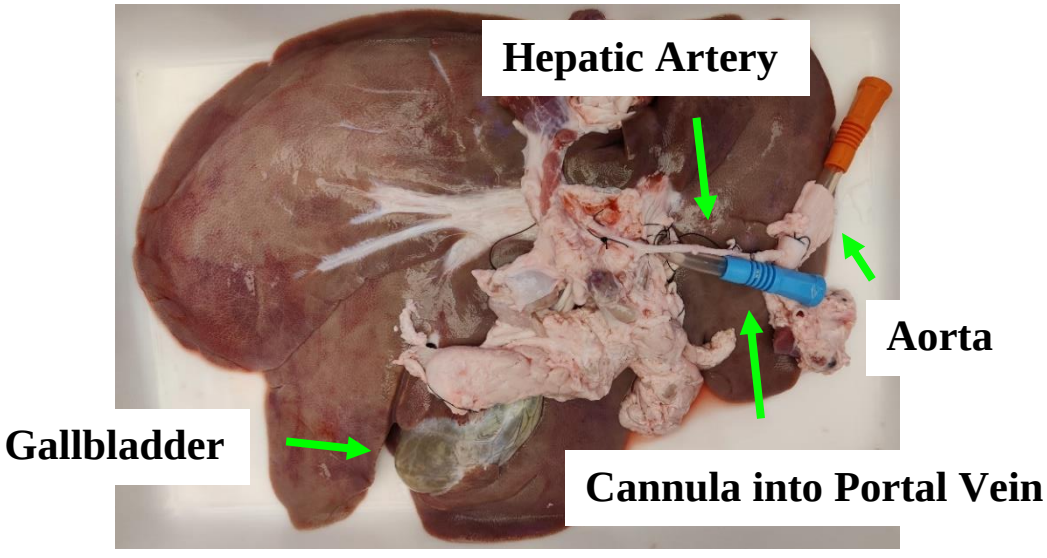

Figure 1. A picture of a porcine liver prepared for perfusion.

A.2 The perfusion of a porcine liver

The goal of the perfusion of the liver, is to keep the anatomical and physiological states of the liver as constant as possible during the experiment, which could be over 6 hours long. This paragraph will give a summary of the essential components necessary for the perfusion of a porcine liver. Additionally, an outline of the possible methods to check the viability of the liver during perfusion is provided [35], [47].

Perfusion components

For perfusion, it is not necessary that the liver is submerged in blood. Therefore, the liver can be placed above a reservoir … see Figure 2. The liver has a darker colour in Figure 2 than in Figure 1 due to blood flowing through the liver. Further, as can be seen in Figure 2, the blood flows in through the cannulas and can freely flow out of the liver on the bottom into the reservoir. To ensure stable perfusion of the liver, at least 5L pig blood is required to fill all the tubing and the reservoir to its minimal level. Also, to prevent coagulation and provide energy, heparin and glucose is added to the blood.

The flow is provided by two pumps. One for the arterial side and the other for the venous side. The flowrates should be around 0.25 ml/min/g liver and 0.75/min/g liver respectively. When providing a pulsatile flow, the arterial flowrate should be between 0.2-0.3 ml/min/g liver. As a clear rule of thumb, the venous flow rate should at least be 3 times as high as the arterial flowrate. This can be measured with flow sensors. When interested in the flow directly going to the liver, measurements could be performed along the tubes directly connected to the liver.

Further, to best resemble the in-vitro situation, the liver should be normothermic perfused at 37 °C. Since the liver was cooled during preparation, the resistance in the liver will drop at the start of the warm perfusion, as the blood vessels open up. The temperature is regulated by originators, which also provide oxygen to the blood. The arterial oxygen supply should be in the range of 0.25-0.5 L/min and the venous supply should be between 0.75-1.5 L/min.

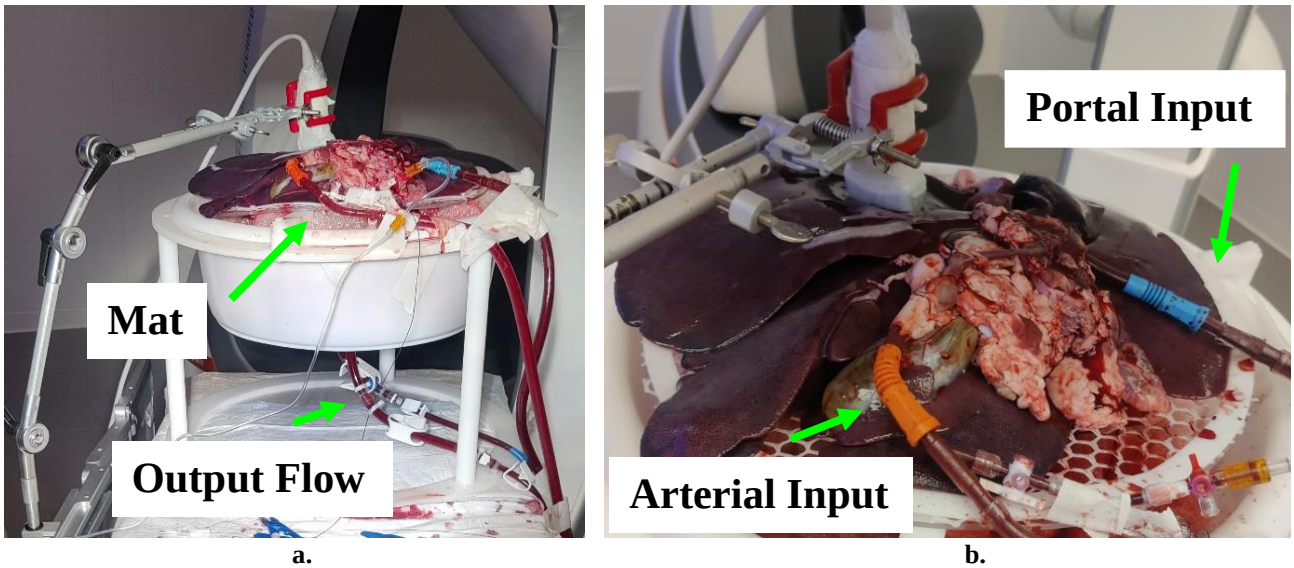

a. **b.**

Figure 2. Overview of the liver during perfusing. **a.** The liver placed on a reservoir is shown. Besides, the so called ‘Mat’ on which the liver rests is indicated, together with the outflow tubes. **b.** A close-up of the liver is shown in.

Viability Check

The hemodynamic parameters such as blood flow can be monitored using the flow sensors. When changes in the flow rates occur the pump settings can be altered to regulate the values. However, to gain more insight why these changes take place, blood gas parameters need to be measured.

For more information about the viability of the liver based on blood gas parameters, blood analyses should be performed before perfusion. Once every 15 minutes during the first hour of perfusion and, depending on the stability of the values, every 30-60 minutes from there on.

Finally, depending on the experiment performed on the ex-vivo perfused porcine liver, the viability could also be checked by imaging modalities. For example, with MRI and US the homogeneity or intensity of contrast-enhanced measurements in the parenchyma of the liver over the duration of the experiment could be compared.

Appendix B | The development of a DCE-US phantom

B.1. Introduction

For the developed algorithms for real-time analysation of DCE-US clips, a platform to generate DCE-US data and test the algorithms would be necessary for fast iterative improvement of the algorithm. Unfortunately, using porcine livers for the development of the algorithm would be too laborious and impede the improvement of the algorithm.

Therefore, a simple phantom could be the solution, if it mimics the liver parenchyma to the extent that DCE-US measurements would result in representative TICs. In order to do so, the phantom should simulate the wash-in and wash-out of microbubbles in the microvasculature and be ultrasound compatible. Furthermore, to overcome the limitations of using porcine livers for the validation of the DCE-US analysis algorithms, the phantom should be fast to set up and easy to work with.

In this appendix, the development and validation of a DCE-US compatible microvasculature mimicking fantom will be described.

B.2. Methods

In this section, the general idea of the fantom will be introduced first, followed by a more detailed description per element. At the end of this section, the methods for validating the phantom are described.

General setup design

For the design of the fantom inspiration was found in the work of P. Chen et all. (2019), who described an open circuit tissue-mimicking phantom used for DCE-US measurements [48]. An open circuit has the benefit of a straightforward control over the flow rate and the microbubble concentration in the phantom. Furthermore, the microvasculature can be mimicked by spaces between alginate beads. A schematic overview of the setup is given in Figure 1.

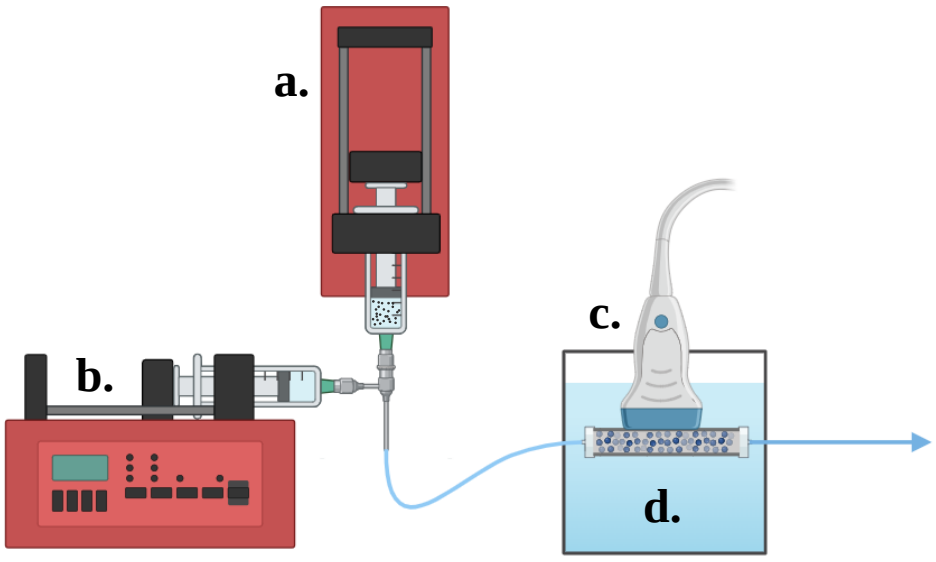

Figure 1. A schematic overview of the setup. **a.** Syringe pump for injecting microbubbles. **b.** Syringe pump for producing the main flow through the phantom. **c**. Indicates the positioning of the ultrasound transducer. **d.** Indicates the phantom placed in a water bath. The outflow was collected in a beaker.

Creation of alginate beads

Alginate is a polymer extracted from seaweed, which can form a gel when dissolved in water. Alginate is stable, biodegradable and save, as it is for example approved to be used in food. When a 2% alginic acid sodium salt solution is pipetted into a 5% calcium chloride solution, small gel beads will form, see Figure 2. After pipetting drop by drop, the beads will first float close to the surface and after a couple of minutes sink to the bottom if the chemical formation of the gel is completed. The resulting size of the beads depends on the needle size, used to pipet the alginic acid sodium salt solution, see Table 1.

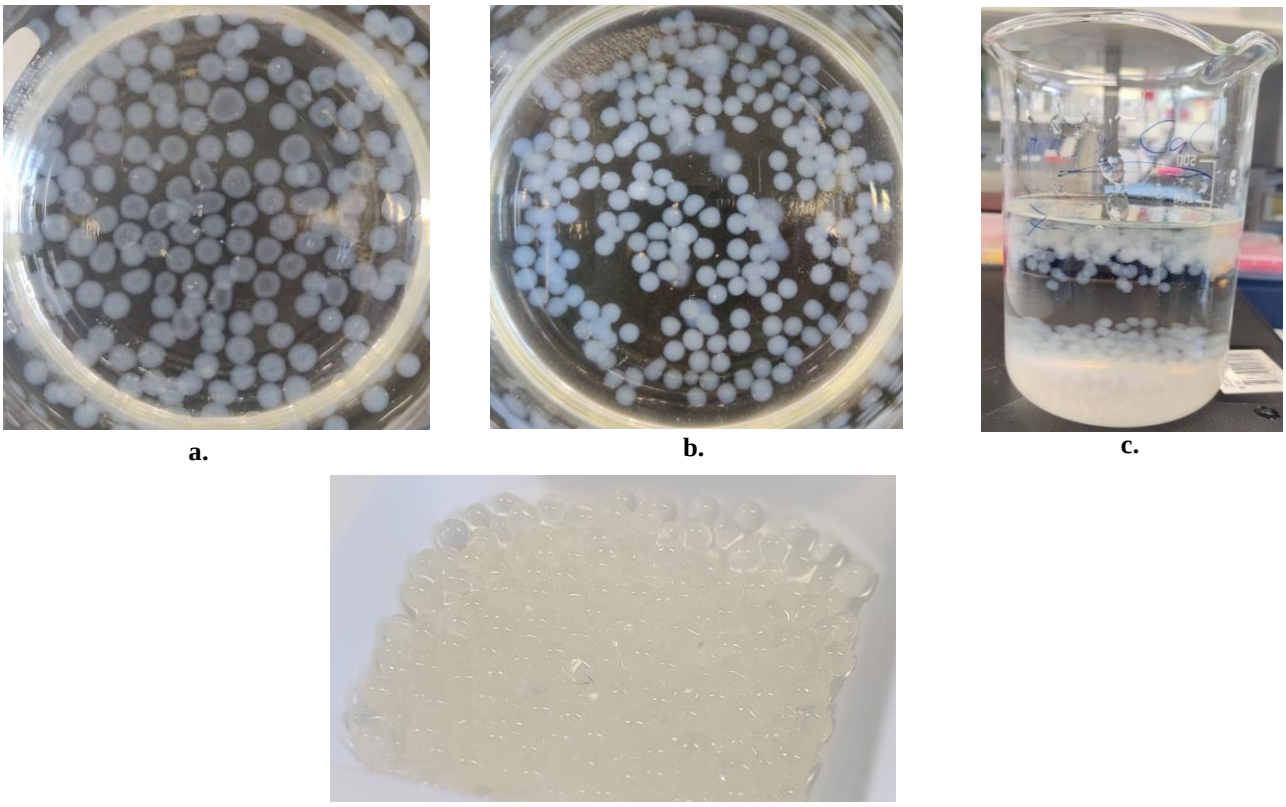

Figure 2. An overview of the steps in the process of creating beads is shown. **a.** Shows the alginate beads after pipetting. The colour difference between the core and the edge of the beads shows that not all material has finished reacting. **b.** Shows the same beads as in a. a couple minutes later. All the material in the cores has now undergone a chemical reaction. **c.** Shows how beads which are finalised can be distinguished from beads which are forming, as they sink to the bottom of the beaker when they are ready. **d.** Shows an image of 'dry' 3 mm alginate beads.

Table 1. Resulting bead size based on the pipetting method.

Bead Diameter [mm]	**Method used for pipetting**
0.2 – 0.5	Tapping on a 30G needle
1.2 – 1.5	Gravity fall from a 30G needle
2.6	Gravity fall from a 21G needle
3.0 – 4.0	Gravity fall directly from a 1 mL Syringe

Microvasculature as a space between alginate beads

The size of spaces between the alginate beads, which can mimic the microvasculature, depend on the size of the alginate beads. For example, the most dense 2D configuration of 3 mm beads theoretically would result in a channel of 0.46 mm or 460 µm, see Figure 3. Which is roughly hundred times the size of a capillary. A lesser dense configuration would already result in a three times bigger channel of 1.24 mm. Therefore, 3 mm beads seem too big to produce a suitable fantom. However, P. Chen et all. (2019) showed resulting TICs from DCE-US measurements on fantoms with 3.1 mm, 2.5 mm and 1.6 mm beads. All sizes resulted in a measurable

wash-in and wash-out of microbubbles. However, with a decreasing bead size, the resistance of the fantom increases, which may cause microbubbles to collapse, due to the higher injection pressure. Besides, air-bubbles can get trapped between the beads. In DCE-US measurements, these air-bubbled cause artefacts. If smaller beads are used, the fantom will consist of more beads and therefore have more potential locations where air-bubbles may stick. Therefore, 3.0 – 4.0 mm beads pipetted with a 1 mL syringe were used in the first proof-of-concept test of this fantom.

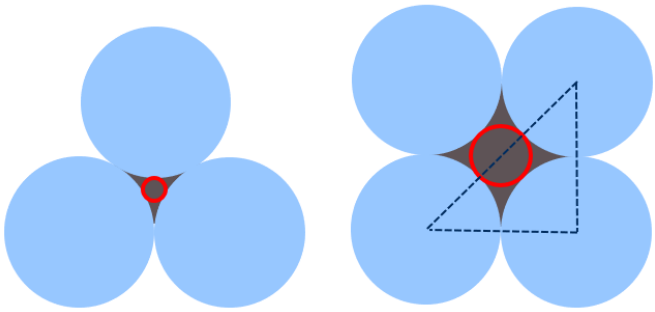

a. **b.**

Figure 3. Two bead configurations and their theoretical resulting microvasculature. **a.** The densest configuration of 3 mm alginate beads (blue) would result in a 0.46 mm channel (red). **b.** A less dense configuration would result in a 1.24 mm channel. The calculation can be solved by Pythagoras, as indicated by the dotted rectangle.

Ultrasound compatible tubing

The tubing holding the microbeads should be ultrasound compatible. One way to lower the influence of the tubing on the measurements would be to make it as thin as possible. Further, the material properties play a role. One of the material options is flexible 80a resin, which is transparent and can be 3D printed in the desired thickness and length. Further, the acoustic properties seemed favourable [49]. Therefore, this material was tested first. To fit nicely with an ultrasound probe, a 12 cm long tube with an inner diameter of 15 mm was printed, see Figure 4. The wall thickness could be limited to 1 mm before running into printing limitations.

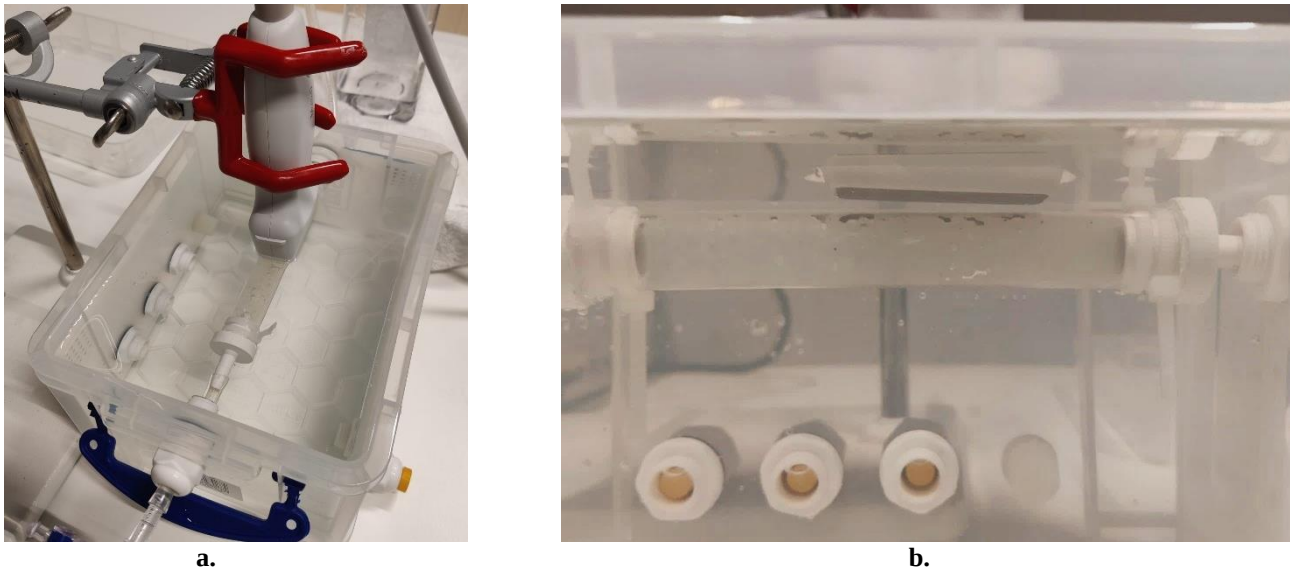

a. **b.**

Figure 4. The combination of the fantom with an ultrasound probe is shown. **a.** top view. **b.** side view.

Syringe pumps

The flow was provided by a syringe pump (PHD ULTRA, Harvard Apparatus, Holliston, United States) equipped with two 60 mL syringes. The microbubble injection could be performed with a second syringe pump (SyringeTWO, New Era Instruments, New York, United States). The flowrates and injection volumes could be set separately.

Connection pieces

To connect the whole setup 3/16 inch clinical tubing was used. Because of the size this tubing is compatible with syringes and 3-way valves. For the connection of the microcirculation mimicking phantom to the rest of the setup, 3D printed PLA connector pieces where designed, see Figure 5. These connector pieces also contained a 1.4 mm filter, to keep the microbeads in place.

Figure 5. An image of the inside of one of the two PLA connector pieces is shown.

Validation of the fantom

The validation of the fantom is examined with three different tests: volume measurements, coulter counter measurements and DCE-US measurements. Additionally, for demonstrating purposes, the resulting TICs from a some DCE-US test measurements on the phantom are shown.

Volume measurements A simple test to get a rough estimate of the resulting size of the spaces between the microbeads, is to measure remaining volume inside the tube by filling it with water. As the length of the tube and its diameter are known, the total space between the alginate beads per cross-section can be calculated. When this is divided by the number of channels between the beads and the tube, a gross indication of the size of the 'vessels' is obtained. Assuming the arrangement shown in Figure 6, there would be 36 channels. As the microbeads and the tubing are elastic, the space between the beads and the tubing as shown in Figure 6 would be probably less.

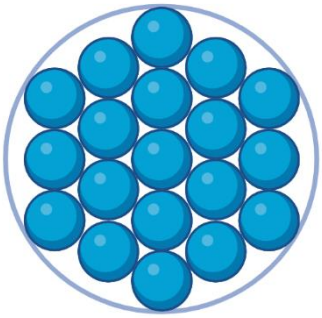

Figure 6. A hypothetical configuration of the 3.0 mm alginate beads inside the 15 mm tube is shown.

Coulter counter measurements To ensure that the microbubbles stay intact when passing through the fantom, a pre- and post- particle size distributions were measured with a coulter counter. The volumetric size distribution of the bubbles available for this experiment is shown in Figure 7. In Figure 7, it is visible that the mixture consists of a combination of monodisperse bubbles of an average diameter of 5 and 7.5 μm. The dotted line is plot as a reference for comparing the results.

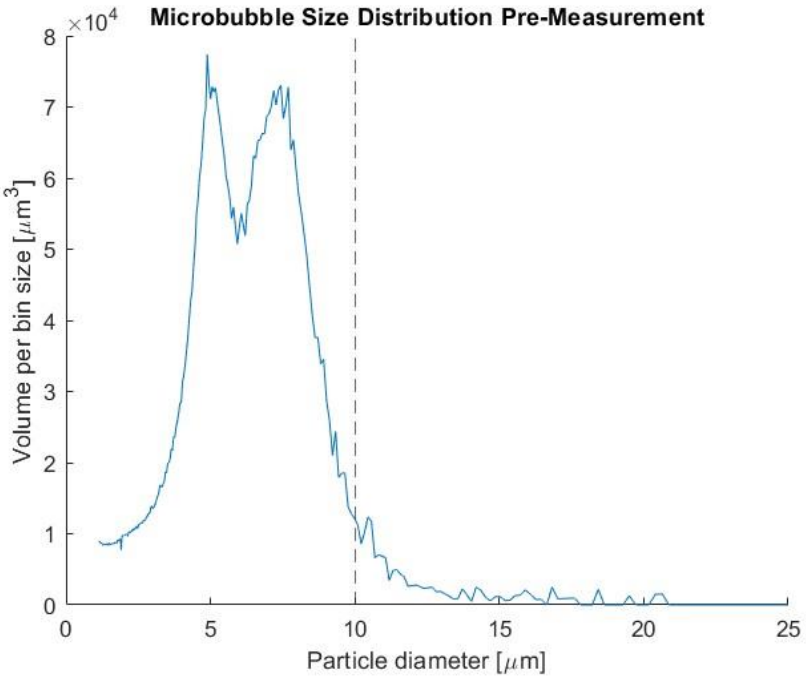

Figure 7. The volumetric size distribution of the bubble used for the experiment is shown.

DCE-US measurements To test the ultrasound compatibility of the 1.0 mm flexible 80a resin tube, four DCE-US recordings were made with a microbubble concentration ranging from 1:5 until 1:5000, while the injected volume remained constant. The measurements were performed with a 9L4 probe (Siemens Healthineers, Erlangen, Germany) placed slightly above the fantom, see Figure 4. In this way, air bubbles sticking to the probe which could potentially lead to artifacts could be removed.

TICs To demonstrate the TICs resulting from the DCE-US measurements on the fantom, ten test measurements where analyses. The same setups as shown in Figure 4 was used. The general flow through the phantom was set at 0.5 ml/seconds. Microbubbles were injected with a rate of 0.04 ml/second over 10 seconds. The starting microbubble concentration was 1:25. However, as the valve towards the microbubble syringe was not closed between measurements, the microbubble mixture was diluted over time.

B.3. Results

Volume measurements

There was 4.2 mL needed completely fill the resin tube including the beads. As the tube was 12 mm long, this results in a general cross-section-area in between beads of 35 mm^2. As it was estimated to have 36 channels per cross-section, this would roughly result in 1 mm^2 per channel. This would approximately result in radius of 0.5 mm.

Coulter counter measurements

The volumetric size distribution of the microbubbles who passed the fantom is shown in Figure 8. When referring to the dotted line at the same location as in Figure 7, it is visible that the distribution shifted to the right, which indicates the disruption of microbubbles.

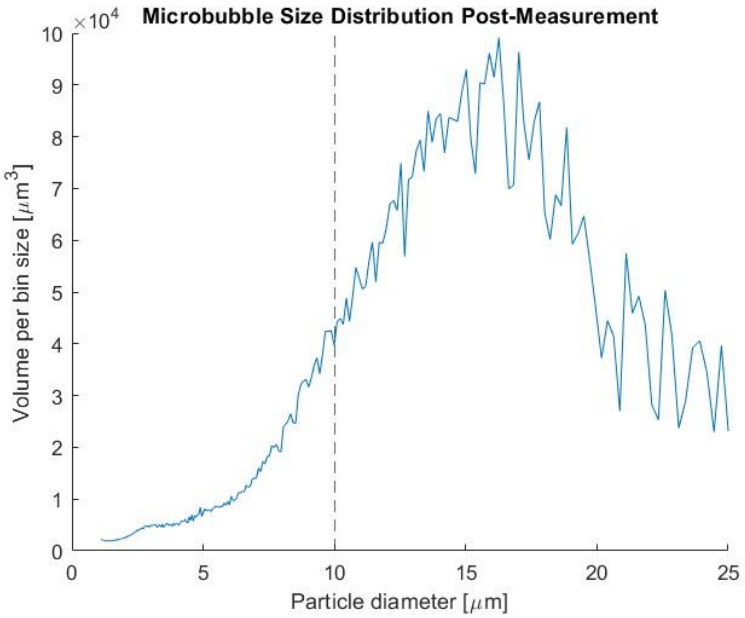

Figure 8. The volumetric size distribution of the bubble who passed through the fantom are shown.

DCE-US measurements

The result of the four DCE-US recordings with a microbubble concentration ranging from 1:5 until 1:5000 are shown in Figure 9. Since the different microbubble concentrations can be distinguished by means of different enhancements, it can be concluded that the resin tube can be used for these types of measurements.

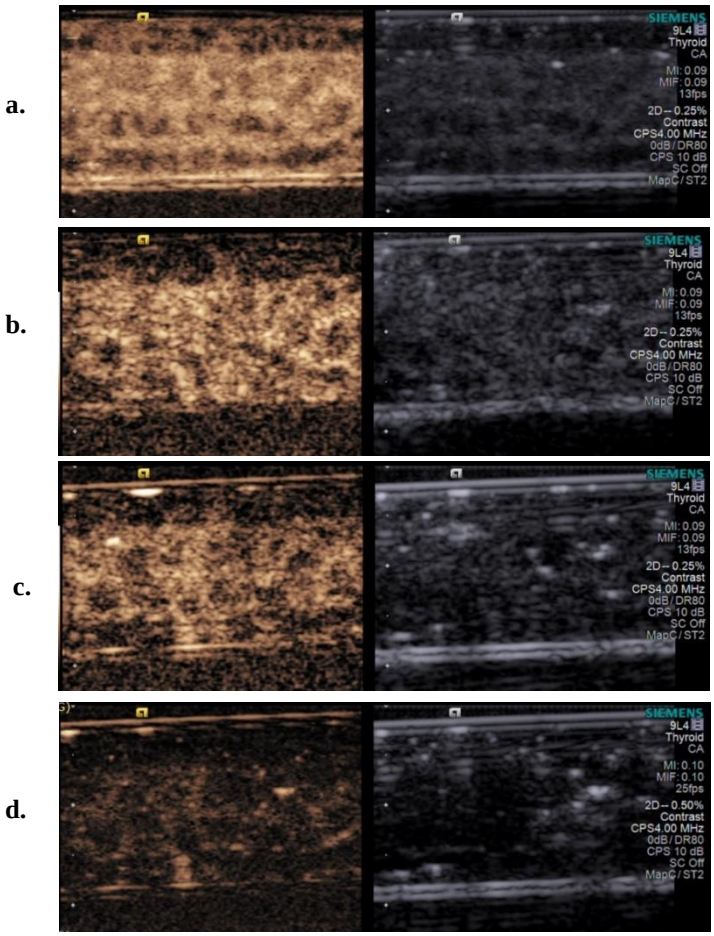

Figure 9. DCE-US recordings with varying microbubble concentrations.

TICs

The test resulting TIC from the analysis of the test measruments are shown in Figure 10. The graphs reach lower PIs over time.

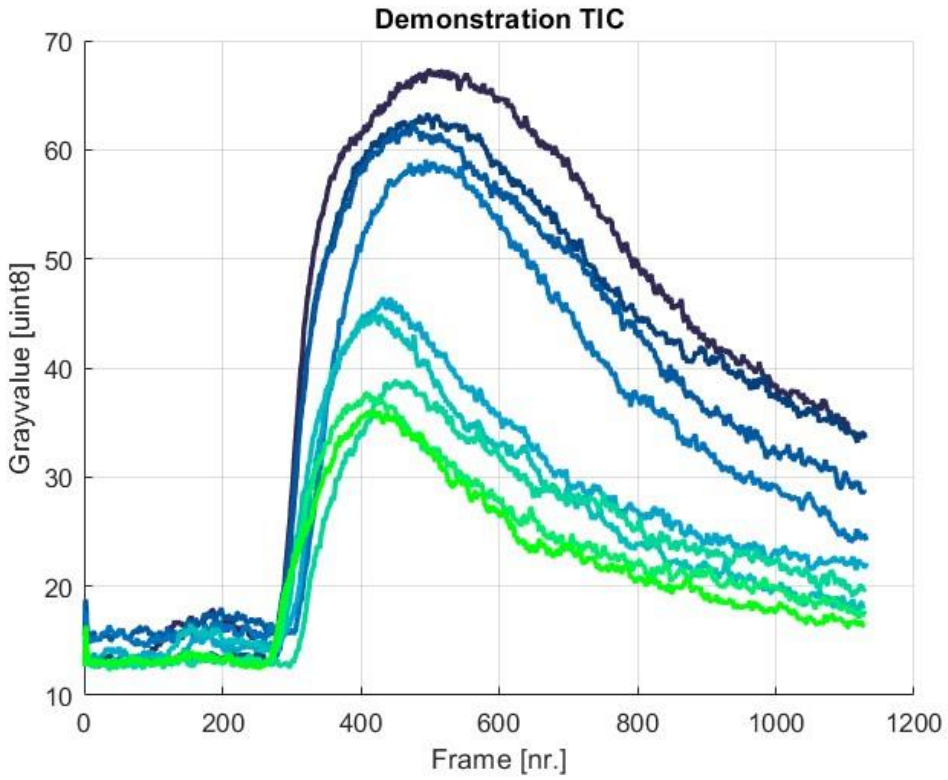

Figure 10. TICs resulting from DCE-US measurements on the fantom. The colour represent the order in which the DCE-US recording resulting in the TICs where recorded, from dark blue (first measurement) until light green (last measurement). The microbubble mixture use for the measurement was more diluted over time.

B.4. Discussion

A DCE-US compatible vasculature mimicking phantom was designed and developed. It should be noted that the average diameter of the “vessels in the phantom is roughly 1 mm, which is larger than a true capillary. Besides, from the coulter counter measurements it is clear that a considerable number of microbubbles rupture when they are injected in and passing through the phantom.

In spite of its limitations, when performing DCE-US on the phantom, a wide range of microbubble concentration could be recorded with limited interference of the 1.0 mm resin tubing. Further, it is shown that DCE-US recordings of the phantom can result in TICs with typical wash-in and wash-out characteristics. Besides, the resulting images and TICs where comparable with literature [48].

In future experiments, the cause of the rupturing of the microbubbles could be investigated and possibly prevented by, for example, changing the general flow rates. Further, combining beads of multiple sizes could result in a more diverse phantom.

It can be concluded that a phantom suitable for the development of an algorithm for real-time analysation of DCE-US recordings was created.

Appendix C | The translation factor

C.1 Introduction

The microbubble concentration in an ROI can be estimated based on the received pressures by the ultrasound probe [25]. However, as the raw data is often not made available by the ultrasound scanner, the log-compressed, gamma transformed and colour coded pixel intensity data needs to be reverse engineered [26]. Unfortunately, as the values of the variables needed for these calculations are also hidden, currently the most viable way to retrieve the backscattered pressures is to rely on commercially available software like VueBox (Bracco Suisse, Geneva, Switzerland).

Through licenses, Vuebox has access to the vendor specific required information to perform the back-calculation. Based on DICOM clips of DCE-US measurements, Vuebox can calculate the PI in dB. Based on this value, the microbubble concentration in an ROI can be estimated. However, when using VueBox, it is not possible to do this real-time [34]. Therefore, a real-time strategy to estimate the microbubble concentration is still lacking.

A possible solution could be to find a fit that describes the translation between pixel intensity data and, through VueBox retrieved, dB data. A translation factor can be applied real-time on pixel intensity data, resulting in the possibility to directly estimate the microbubble concentration in an ROI during DCE-US measurements.

C.2 Methods

A total of 33 DICOM clips of DCE-US measurements recorded in two ex-vivo perfused porcine livers at three positions were analysed with VueBox. The measurement positions are shown in Figure 1. During the measurements at Lob 1, the catheter injecting the microbubbles was positioned at five different locations. At each of the five locations the measurement was repeated three times. During the measurements at Lob 2 and 3, the catheter was located at three different positions and again the measurements were repeated three times at each location.

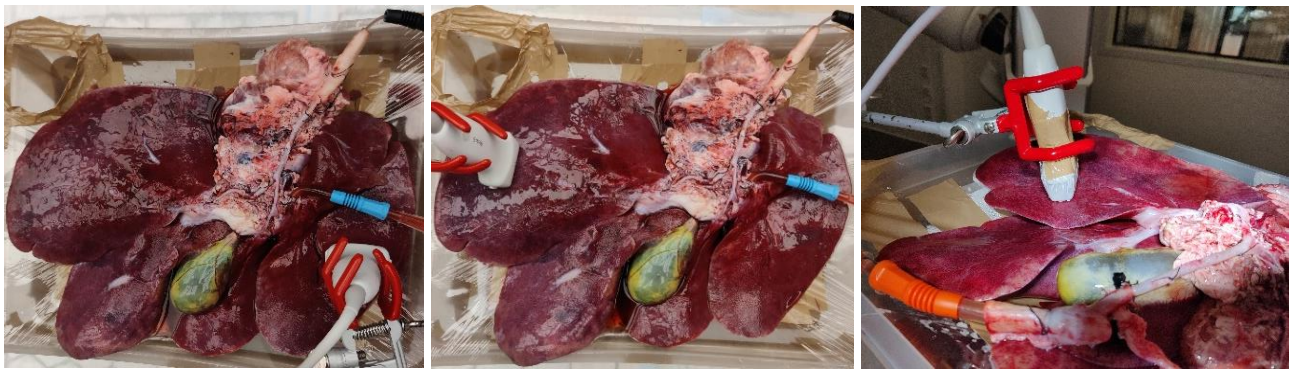

a. Position "Lob 1" **b**. Position "Lob 2**"** **c**. Position "Lob 3"

Figure 1. The three DCE-US recording positions.

After selecting an ROI on the DCE-US recordings and the time of microbubble arrival, VueBox calculated the PI in dB, see Figure 2. A similar analysis was performed in MATLAB (R2023b; The MathWorks, Natick, MA, USA). The same ROI was selected, and the mean intensity of the pixels in the ROI was plotted over time, resulting in a TIC expressed in 8-bit. Next, the time of arrival was selected. The PI was determined as the maximum value of the TIC, minus the intensity value at the time of arrival, similar to the procedure in VueBox, see Figure 3.To find a translation factor between the 8-bit values and the dB values, the values were plotted and the best fit of the relation was found by MATLAB Curve Fitter which minimises the sum of squares errors (SSE). The SSE is calculated as

$$\boldsymbol{SSE = \sum (measurement - fit)\text{^}2}$$

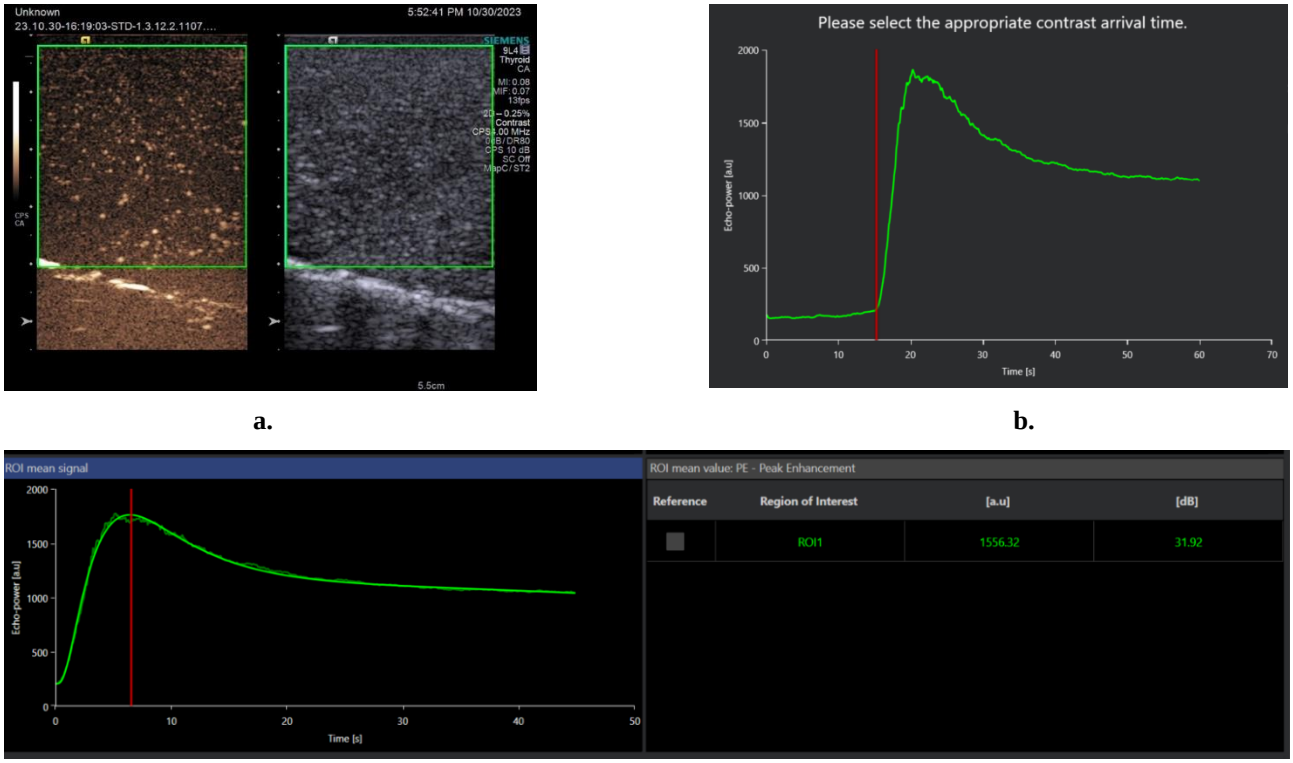

Figure 2. An overview of steps of the analysis in VueBox is shown. The chronological order is from a. until c. **a.** Selection of an ROI in green on a DCE-US recording. **b.** A 'preview' TIC on which the time of **c.** The resulting TIC and the derived PI in arbitrary and dB units.

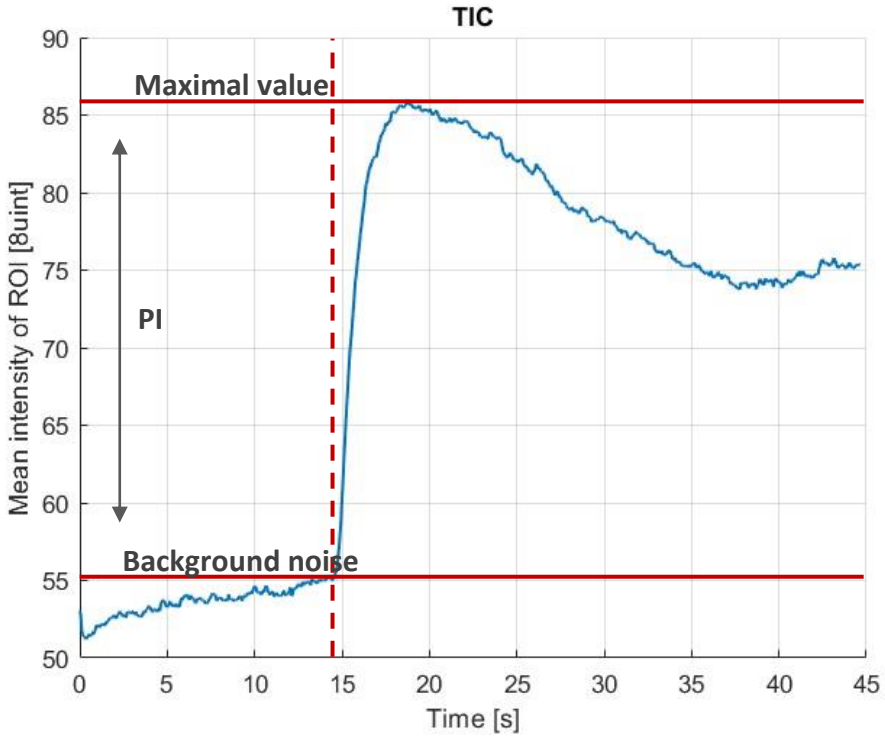

Figure 3. An overview of the TIC analysis performed in MATLAB is shown. The PI is pixel intensity value at the moment of maximal enhancement caused by microbubbles. Therefore, the intensity not caused by microbubbles, the background noise, needs to be subtracted from the maximal value in order to find the PI.

C.3 Results

The resulting PI of each DCE-US measurement in 8-bit and dB is shown in Table 1. According to VueBox the pressure received by the ultrasound probe during the measurements ranged between 28.16 dB and 36.89 dB. This is a difference of 8.73 dB, which corresponds to almost a threefold increase in received pressure from the lowest to the highest PI.

Table 1. An overview of the measurements and the resulting PIs. In the seven measurements which are marked red, a typical wash-in and wash-out was absent in the TIC.

Measurement	**Max Value – MATLAB [8-bit]**	**PI – MATLAB [8-bit]**	**PI - VueBox [dB]**
Lob1_L1_M1	135.6383	98.6525	35.52
Lob1_L1_M2	129.2200	92.3368	35.89
Lob1_L1_M3	124.6341	87.9072	34.62
Lob1_L2_M1	133.8422	94.9389	35.29
Lob1_L2_M2	134.0504	95.3229	35.31
Lob1_L2_M3	144.3170	96.6689	36.89
Lob1_L3_M1	136.4168	93.8653	35.92
Lob1_L3_M2	126.8766	78.7837	35.18
Lob1_L3_M3	124.6721	86.4824	34.74
Lob1_L4_M1	25.2870	-	+Inf
Lob1_L4_M2	100.2689	62.1988	31.19
Lob1_L4_M3	104.9049	63.6810	31.77
Lob1_L5_M1	93.8895	51.9767	30.99
Lob1_L5_M2	96.8407	56.2452	30.33
Lob1_L5_M3	79.8816	39.6591	28.22
Lob2_L1_M1	95.9238	52.4322	31.12
Lob2_L1_M2	90.7092	51.3163	30.67
Lob2_L1_M3	92.6075	51.7300	30.85
Lob2_L2_M1	46.3234	-	14.21
Lob2_L2_M2	45.5180	-	13.07
Lob2_L2_M3	45.2577	-	+Inf
Lob2_L3_M1	95.9238	52.0564	30.28
Lob2_L3_M2	90.7092	53.5328	30.81
Lob2_L3_M3	92.6075	48.8144	30.27
Lob3_L1_M1	96.5287	54.4262	32.18
Lob3_L1_M2	90.9864	46.1329	30.83
Lob3_L1_M3	94.7642	54.6100	31.68
Lob3_L2_M1	49.1895	-	16.38
Lob3_L2_M2	55.0234	-	17.11
Lob3_L2_M3	54.2216	-	18.19
Lob3_L3_M1	76.1237	32.4796	28.16
Lob3_L3_M2	82.3306	44.3361	29.68
Lob3_L3_M3	83.3270	39.8795	29.22

In the TIC of several measurements the typical wash-in and wash-out pattern was absent. This occurred in measurements with a maximum intensity value up to 56 8-bit and lower. As a result, Vuebox gave +Inf or the moment of PI was impossible to determine, see Figure 4.

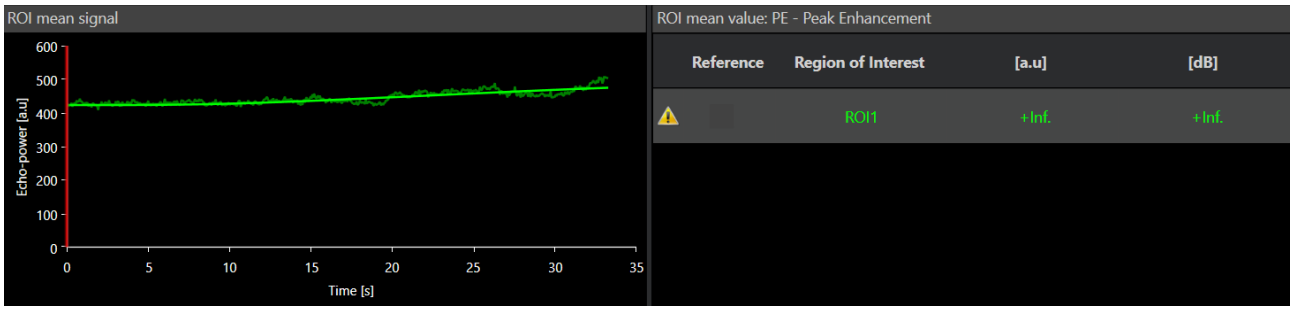

a.

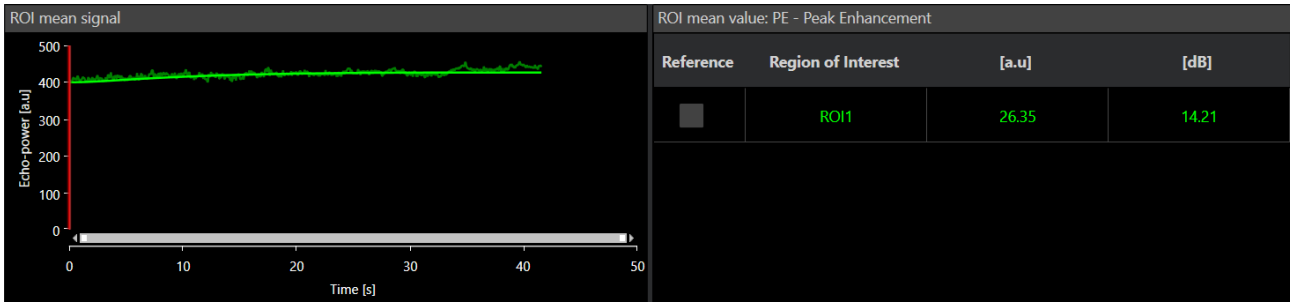

b.

Figure 4. Examples of measurements where the wash-in and wash-out patterns where not present. As a result, the moment of peak enhancement is impossible to distinguish. In some cases, this can cause VueBox to return +Inf as a result. **a**. The TIC of measurement *AntiLob_L2_M3*. **b**. The TIC of measurement *AntiLob_L2_M1*.

Figure 5 shows a plot of the 26 measurements where a typical wash-in and wash-out pattern was present. The PI value of each measurement in dB is shown on the y-axis, and the PI value of the same measurement in 8-bit is shown on the x-axis. The line in red represents the most optimal fit through all the data points. However, only the measurements at position 'Lob' extend above an 8-bit value of 60. As it is deemed important to determine a suitable fit over the whole relevant range of PI values measurable in porcine livers, an alternative fit through only the 'Lob' measurements is calculated and shown in blue. As a compromise between the two fits, the slope of the fits is averaged, which resulted in a translation factor of

$$[\boldsymbol{dB}] = [\boldsymbol{8bit}] * \mathbf{0.12475} + \mathbf{24.5051}$$

The resulting fit is shown in Figure 6 and 7 in two different magnifications in order to get a complete overview of the fit, locally and more generally.

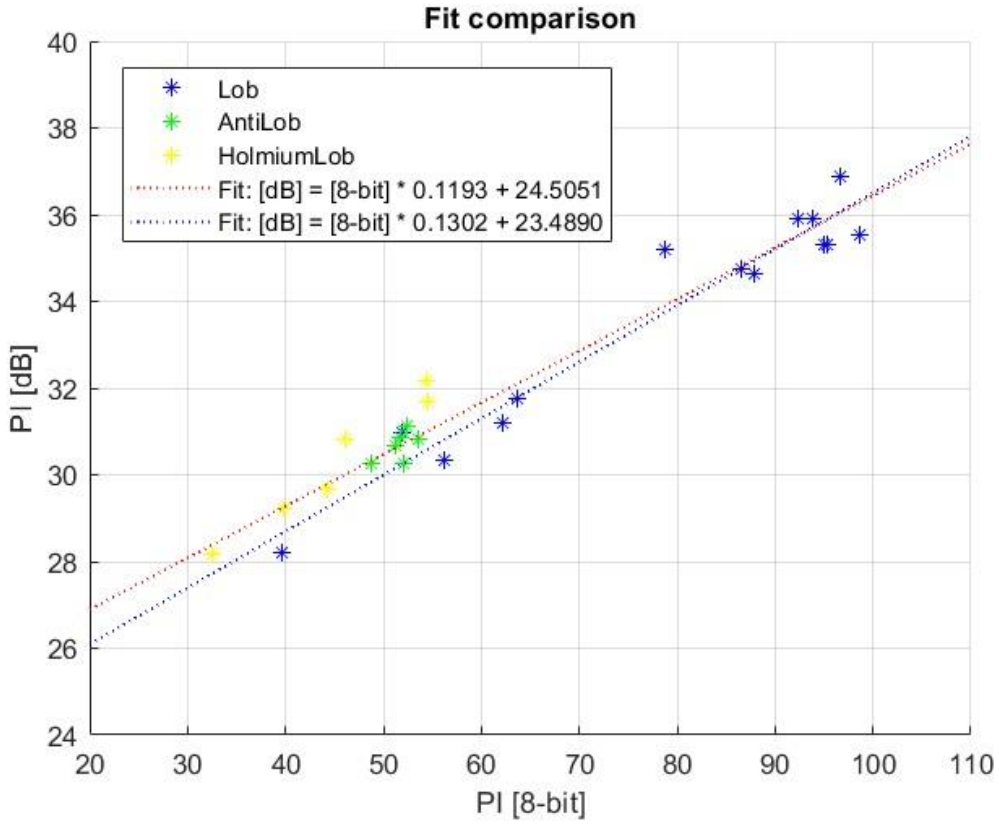

Figure 5. The most optimal fit though all the measurement points is shown in red (dotted line). Additionally, the most optimal fit through only the 'Lob' measurement points is shown in blue (dotted line).

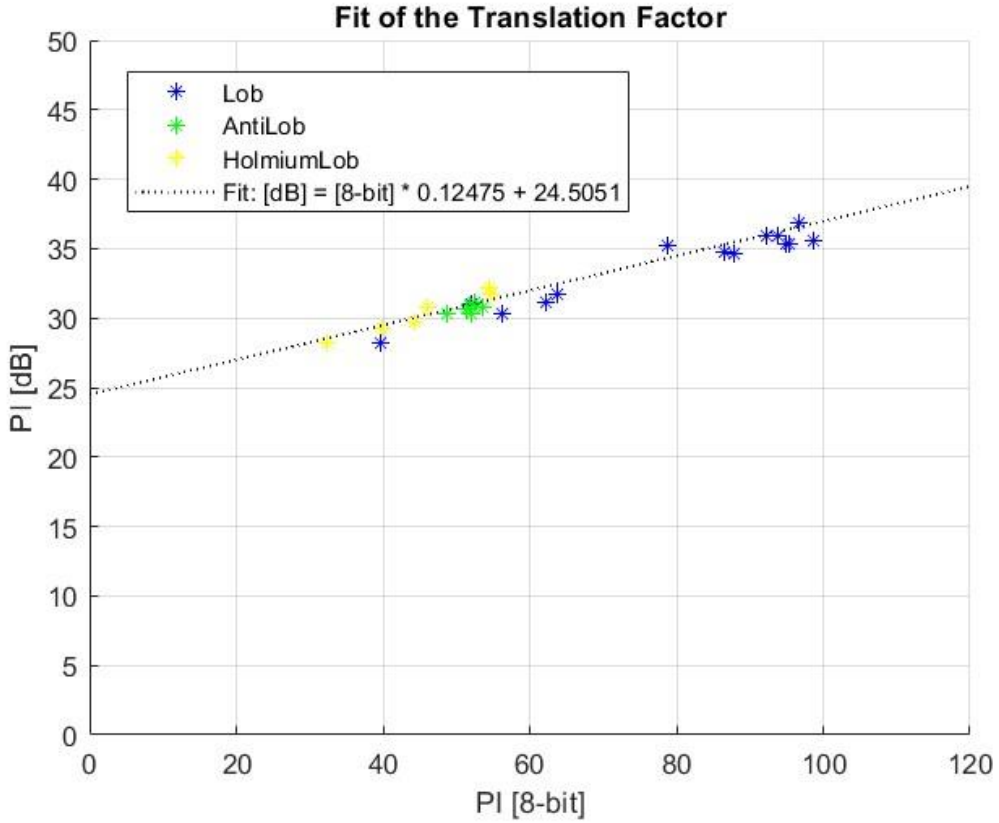

Figure 6. An overview of the final fit is shown from [0,0].

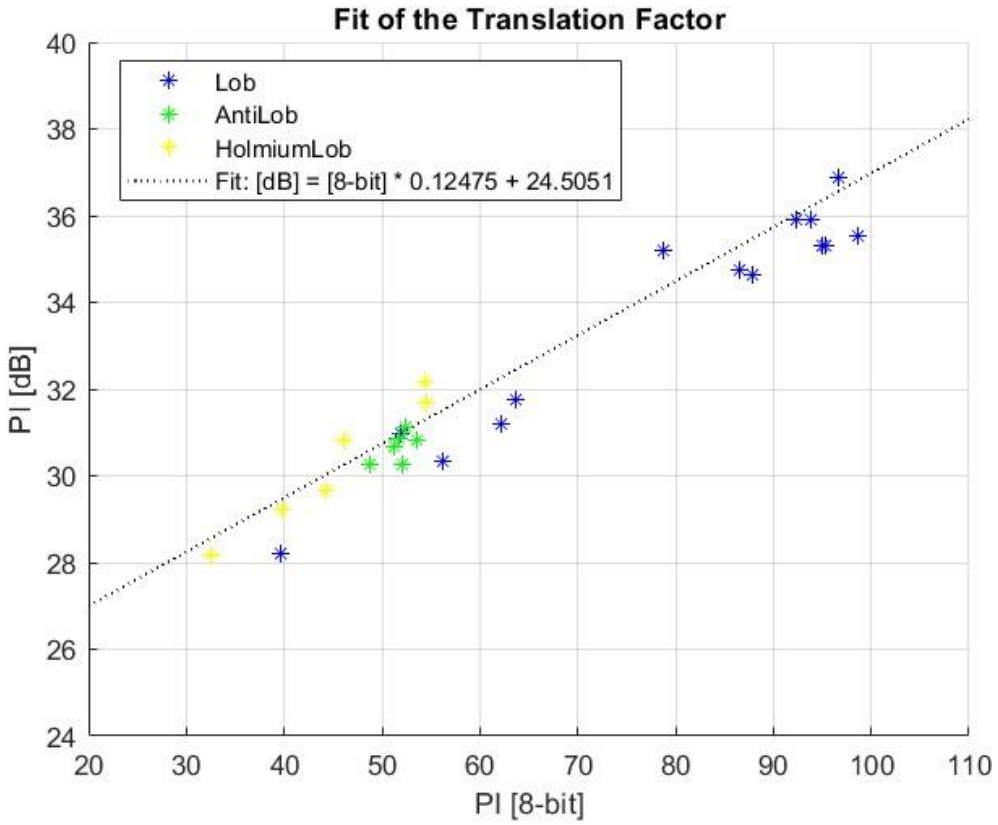

Figure 7. The final fit shown in more detail regarding the measurement points.

C.4 Discussion

Based on previous measurements in ex-vivo perfused porcine livers, a translation factor between the PI in 8-bit and PI in dB could be determined. This factor can be applied during real-time analyses of future DCE-US measurements. However, there are some points of caution which need to be mentioned.

According to this fit an intensity of zero 8-bit would still result in a PI of 24.5051 dB, which is highly illogical. It shows that the fit is unsuitable for data outside the range that was used to obtain it, from approximately 35 until 100 8-bit.

Furthermore, there is a lack of data in the 65 to 85 8-bit range. Currently a linear relation is assumed. However, in future work when more data is available it is recommended that this assumption is reconsidered.

To conclude, a translation factor from PI values in 8-bit to PI values in dB was determined. This enables users to obtain the real-time estimation of a microbubble concentration in an ROI during DCE-US measurements, when a TIC in 8-bit is already available.

Appendix D | Development Gain & Dynamic Range Check

D.1 Introduction

The work of Rognin et all. (2008) showed the importance of a sufficient dynamic range (DR) and suitable gain settings for the reverse engineering of processed US data, to 'raw' data. They compared back-calculated data recorded with different settings to raw data [36]. A DR which is too narrow can cause clipping of the DCE-US signal. The pixels with the lowest intensities are then all given a pure black value and the highest intensities all pure white, while there should be a difference between them. An incompatible gain setting can result in the same phenomenon, as the gain can push the pixel distribution in its entirety too far to the dark or the bright side of the gray-scale range. When the data is compressed in this way, recovering the true values is impossible. Therefore, it is not possible to give an estimation of the microbubble concentration based on the recordings with clipped data. To verify if sufficient settings are used for the DCE-US measurements, a simple histogram of the pixel intensities can be used [36].

D.2 Methods

An algorithm is developed which will check the Gain and DR settings of a DCE-US recording. After the user has selected an ROI, the algorithm automatically plots a histogram of the pixel distribution of the brightest frame. The brightest frame is of interest as the PI depends on it, which can later be correlated to the microbubble distribution in the ROI. Therefore, it is of utmost importance that especially the data at the moment of peak enhancement should not be clipped.

To evaluate the functionality and added value of the information the algorithm provides, it is tested on three DCE-US data sets, all consisting of three measurements. Two data sets are recorded on a tissue-mimicking fantom described in Appendix B, in which the Gain or DR are changed between subsequent measurement. The third data set is obtained from an ex-vivo perfused porcine liver. As it is clearly stated in literature that the DR for DCE-US measurements should be as wide as possible, or at least above 40 dB, only the influence of the Gain is investigated [25][12]. For an impression of the measurement, see Figure 1. During the measurements of one dataset, all other factors besides the gain an DR remained constant. These include microbubble concentration, injection speed, imaging depth, framerate etc.

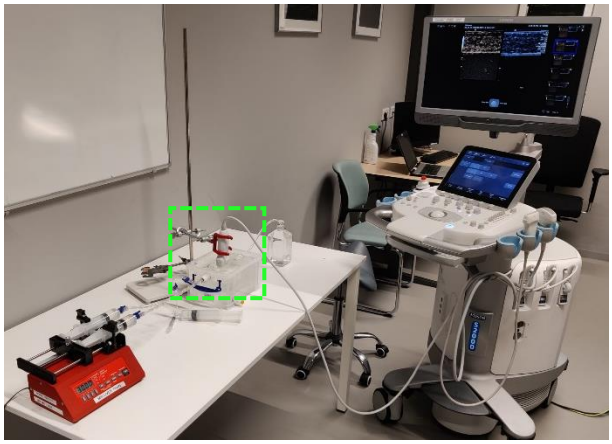

a.

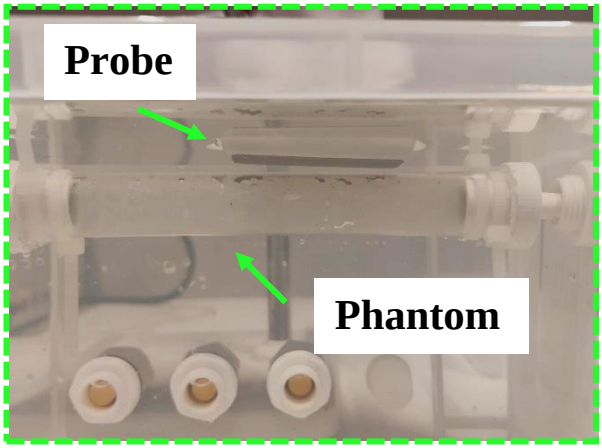

b.

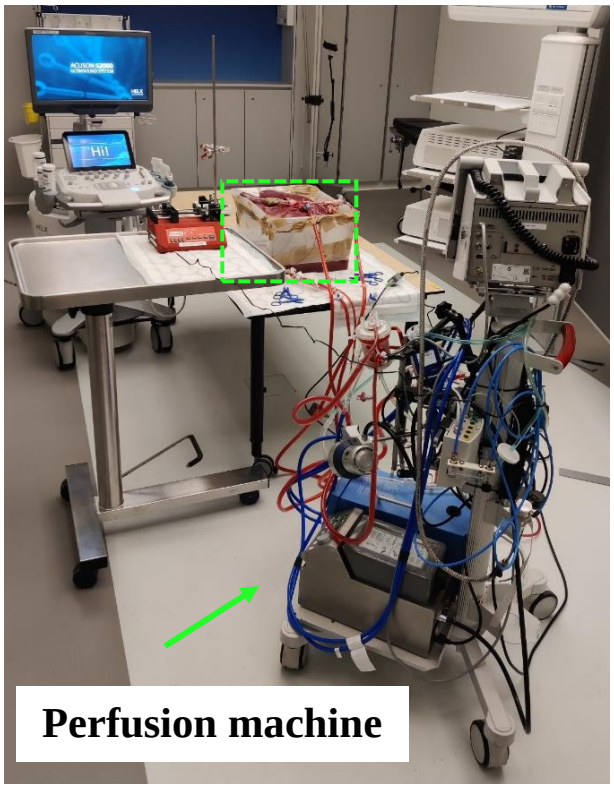

c.

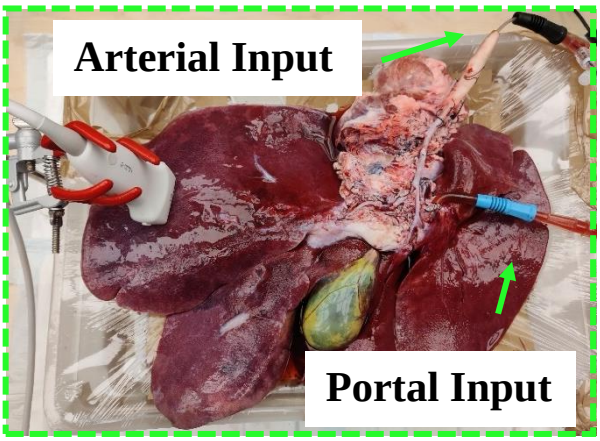

d.

Figure 1. An impression of the in-vitro and ex-vivo measurements is shown. **a.** Shows a general overview of the in-vitro setup, described in Appendix B. **b.** Shows a close-up of the positioning of the probe at the capillary flow mimicking phantom. **c.** Shows a general overview of the ex-vivo setup. **d.** shows a close-up of the positioning of the ultrasound probe on the ex-vivo perfused porcine liver. The arterial input indicates the arterial connection to the perfusion machine. Through the input, the arterial flow is provided. Additionally, a catheter for the microbubble injections is inserted through the input. Via the portal input, the flow through the portal vein and its branches is provided.

D.3 Result

Figure 2 shows the results of the in-vitro measurements where the DR was changed between recordings, the Gain remained constant and was set to 10 dB. In Figure 2a. the clipping of data is clearly visible. There is no noise visible, as a broad range of low value pixels is all set to pure black. This is supported by the blue histogram in 2d, as the pixel intensity distribution is heavily shifted to the left. Despite the 'dull' look with little contrast in 2c, only the combination of DR = 90 and Gain = 10 would result in an unclipped recording. This is shown in the yellow histogram in 2d, as neither the most left nor the rightest bin contain pixels.

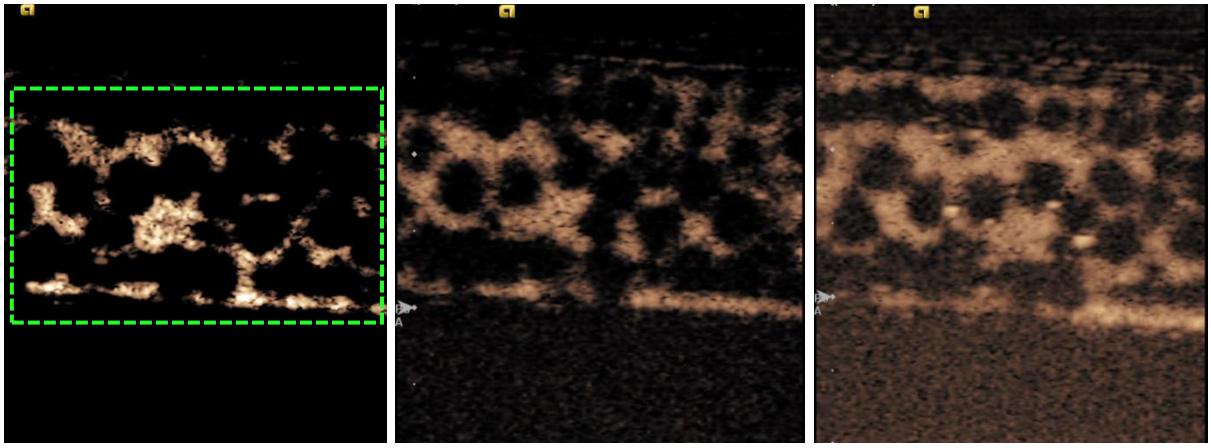

a. Gain = 10, DR = 30 **b**. Gain = 10, DR = 60 **c.** Gain = 10, DR = 90

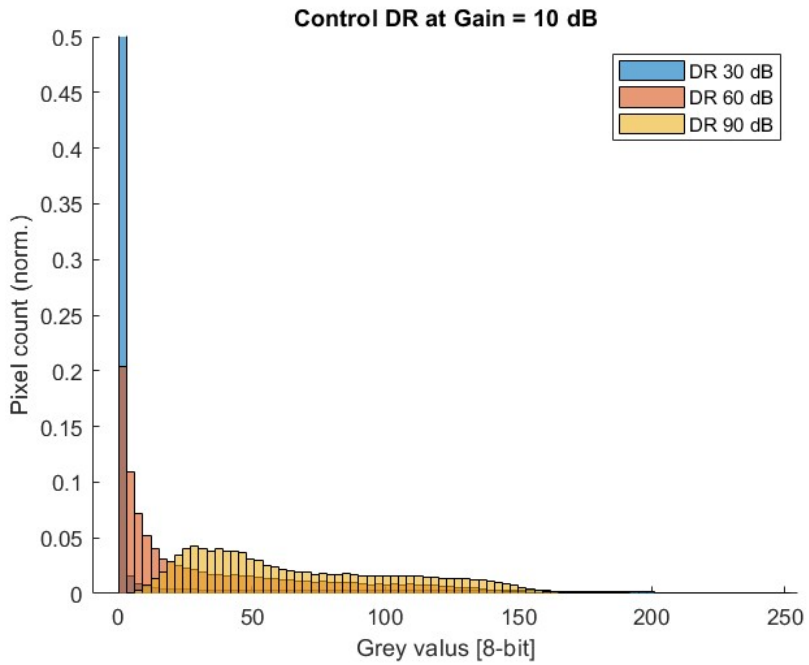

d. Three histograms are plotted which represent the pixel intensity distribution of ROI in a, b and c.

Figure 2. The result of repeated DCE-US in-vitro measurements between are shown, between which the DR was varied. The analysed ROI is indicated by the green square in a.

Figure 3 shows the results of the in-vitro measurements where the Gain was changed, the DR remained constant and set to 90 dB. Despite the 'grainy' look of 3c, the histogram in 3d shows that only a Gain of 10 dB would result in a recording without clipping.

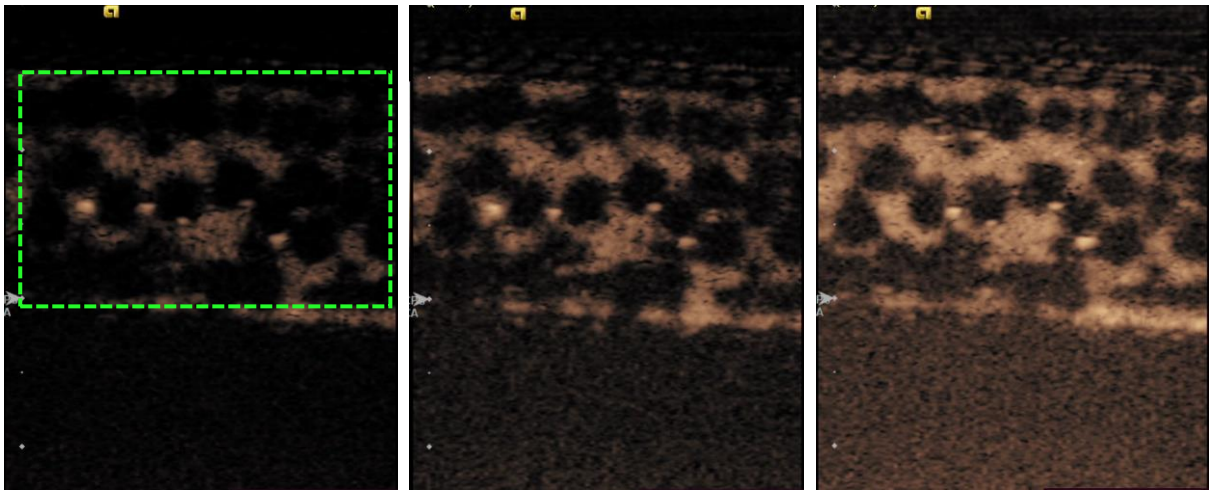

a. DR = 90, Gain = 0 **b.** DR = 90, Gain = 10 **c.** DR = 90, Gain = 20

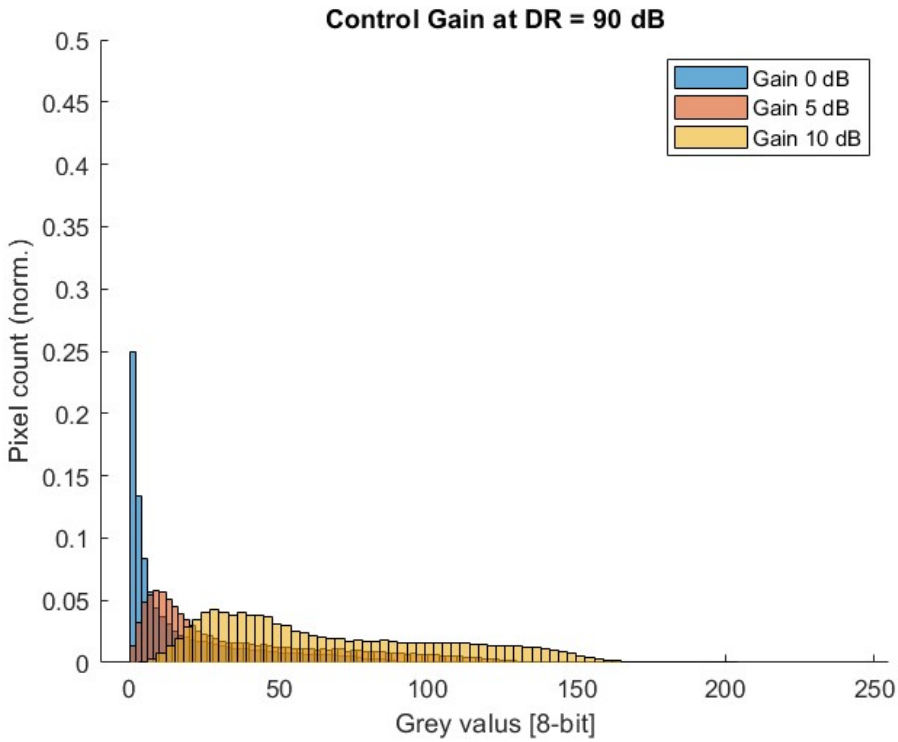

d. Three histograms are plotted which represent the pixel intensity distribution of ROI in a, b and c.

Figure 3. The result of repeated DCE-US in-vitro measurements are shown, between which the gain was varied. The analysed ROI is indicated by the green square in a.

The results of the ex-vivo measurements are shown in Figure 4. From Figure 4 it can be concluded that a Gain of 0 dB is too low, as the blue histogram is heavily weighted to the left. Furthermore, it shows that a Gain of 20 dB is too high, as there is a build-up of pixels in the right-most bin. These pixels needed to be assigned a higher pixel value than there was available. The result is a saturated signal. A Gain of 10 dB results in a balanced signal, as the pixel count of both the most right and left bin is zero.

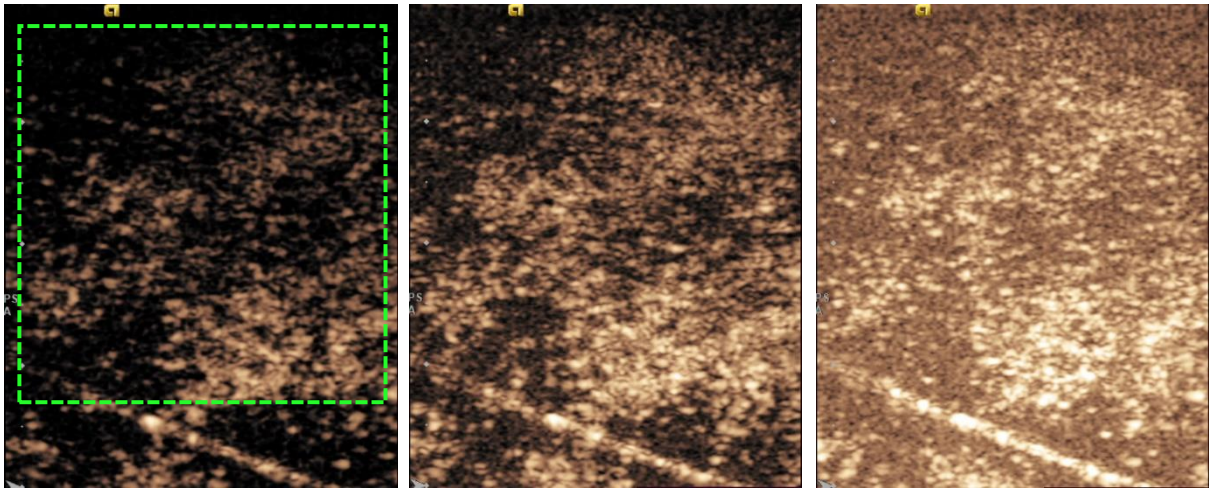

a. DR = 80, Gain = 0 **b.** DR = 80, Gain = 10 **c.** DR = 80, Gain = 20

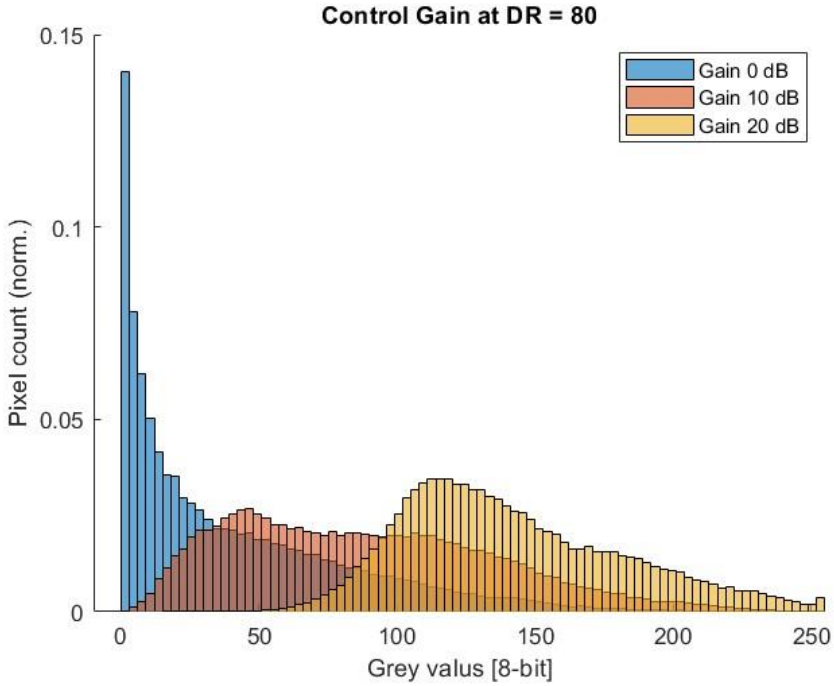

d. Three histograms are plotted which represent the pixel intensity distribution of ROI in a, b and c.

Figure 4. The result of repeated DCE-US ex-vivo measurements are shown, between which the gain was varied. The analysed ROI is indicated by the green square in a.

D.4 Discussion

An automatic algorithm is developed which produces histograms of the pixel intensity distribution over the full available grayscale, to verify if suitable settings are used for DCE-US measurement.

The resulting histograms are comparable with those in literature, and provide information about the influence of the Gain and DR on the quality of the DCE-US recordings [36]. Furthermore, supported by the information that the results of the algorithm provide, the user can make informed choices on the most suitable settings, even though they might seem counterintuitive at first, as they might result in ‘dull’ and ‘grainy’ images.

To conclude, the developed algorithm supports the user in choosing the most suitable DR and Gain settings for recording DCE-US images, which can later be used to estimate the microbubble concentration in the ROI.

Bibliography

[1] H. Sung *et al.*, 'Global Cancer Statistics 2020: GLOBOCAN Estimates of Incidence and Mortality Worldwide for 36 Cancers in 185 Countries', *CA Cancer J Clin*, vol. 71, no. 3, pp. 209–249, May 2021, doi: 10.3322/CAAC.21660.

[2] B. W. Johnson and G. P. Wright, 'Regional therapies for the treatment of primary and metastatic hepatic tumors: A disease-based review of techniques and critical appraisal of current evidence', *The American Journal of Surgery*, vol. 217, no. 3, pp. 541–545, 2019, doi: 10.1016/j.amjsurg.2018.10.018.

[3] D. Anwanwan, S. K. Singh, S. Singh, V. Saikam, and R. Singh, 'Challenges in liver cancer and possible treatment approaches', *Biochim Biophys Acta Rev Cancer*, vol. 1873, no. 1, Jan. 2020, doi: 10.1016/J.BBCAN.2019.188314.

[4] E. Groot Jebbink, 'NOW Talent Programme Veni', 2020. Accessed: Feb. 05, 2024. [Online]. Available: https://www.nwo.nl/en/researchprogrammes/nwo-talent-programme/projects-veni/2020

[5] M. Stella, A. J. A. T. Braat, R. van Rooij, H. W. A. M. de Jong, and M. G. E. H. Lam, 'Holmium-166 Radioembolization: Current Status and Future Prospective', *Cardiovasc Intervent Radiol*, vol. 45, no. 11, pp. 1634–1645, Nov. 2022, doi: 10.1007/s00270-022-03187-y.

[6] P. D. Sutphin, D. Lamus, S. P. Kalva, J. Li, and I. R. Corbin, 'Interventional Radiologic Therapies for Hepatocellular Carcinoma: From Where We Began to Where We Are Going', in *Hepatocellular Carcinoma: Translational Precision Medicine Approaches*, Humana Press, 2019, pp. 169–194. doi: 10.1007/978-3-030-21540-8_9.

[7] A. L. Hermann *et al.*, 'Relationship of tumor radiation–absorbed dose to survival and response in hepatocellular carcinoma treated with transarterial radioembolization with 90Y in the SARAH study', *Radiology*, vol. 296, no. 3, pp. 673–684, Sep. 2020, doi: 10.1148/radiol.2020191606.

[8] Cremonesi M *et al.*, 'Radioembolization of hepatic lesions from a radiobiology and dosimetric perspective', *Front Oncol*, vol. 4, Aug. 2014, doi: 10.4172/2155-9619.1000122.

[9] J. Aramburu, R. Antón, A. Rivas, J. C. Ramos, B. Sangro, and J. I. Bilbao, 'Computational particle-haemodynamics analysis of liver radioembolization pretreatment as an actual treatment surrogate', *Int J Numer Method Biomed Eng*, vol. 33, no. 2, Feb. 2017, doi: 10.1002/CNM.2791.

[10] M. L. J Smits *et al.*, 'Holmium-166 radioembolisation in patients with unresectable, chemorefractory liver metastases (HEPAR trial): a phase 1, dose-escalation study', *Articles Lancet Oncol*, vol. 13, no. 10, pp. 1025–1059, 2012, doi: 10.1016/S1470-2045(12)70334-0.

[11] J. Van der Hoek, T. Snoeijink, H. Mirgolbabaee, and E. Groot Jebbink, 'Analysis of microbubble and holmium-165 microsphere behaviour in a 2D in-vitro liver vasculature phantom', *[Unpublished manuscript]*.

[12] C. F. Dietrich, M. A. Averkiou, J. M. Correas, N. Lassau, E. Leen, and F. Piscaglia, 'An EFSUMB introduction into dynamic contrast-enhanced ultrasound (DCE-US) for quantification of tumour perfusion', *Ultraschall in der Medizin*, vol. 33, no. 4, pp. 344–351, 2012, doi: 10.1055/S-0032-1313026/ID/JR047-13/BIB.

[13] J. Ralph, K. Ahmed, G. Riad, S. Robert, and J. Lewandowski, 'Transarterial Radioembolization with Yttrium-90 for the Treatment of Hepatocellular Carcinoma', *Adv Ther*, vol. 33, no. 5, pp. 699–714, May 2016, doi: 10.1007/s12325-016-0324-7.

[14] A. Vogel *et al.*, ‘Updated treatment recommendations for hepatocellular carcinoma (HCC) from the ESMO Clinical Practice Guidelines’, *Annals of Oncology*, vol. 32, no. 6, pp. 801–805, Jun. 2021, doi: 10.1016/j.annonc.2021.02.014.

[15] A. Kennedy, D. Coldwell, B. Sangro, H. Wasan, and R. Salem, ‘Radioembolization for the treatment of liver tumors: General principles’, *American Journal of Clinical Oncology: Cancer Clinical Trials*, vol. 35, no. 1, pp. 91–99, Feb. 2012, doi: 10.1097/COC.0B013E3181F47583.

[16] I. Xenogiannis, C. Varlamos, T. R. Keeble, A. S. Kalogeropoulos, and G. V. Karamasis, ‘Ultrasound-Guided Femoral Vascular Access for Percutaneous Coronary and Structural Interventions’, *Diagnostics*, vol. 13, no. 12, Jun. 2023, doi: 10.3390/DIAGNOSTICS13122028.

[17] F. Kolligs *et al.*, ‘Factors impacting survival after transarterial radioembolization in patients with hepatocellular carcinoma: Results from the prospective CIRT study’, *JHEP Reports*, vol. 5, no. 2, Feb. 2023, doi: 10.1016/J.JHEPR.2022.100633.

[18] E. Fröhlich, R. Muller, X. W. Cui, D. Schreiber-Dietrich, and C. F. Dietrich, ‘Dynamic Contrast-Enhanced Ultrasound for Quantification of Tissue Perfusion’, *Journal of Ultrasound in Medicine*, vol. 34, no. 2, pp. 179–196, Feb. 2015, doi: 10.7863/ULTRA.34.2.179.

[19] C. F. Dietrich *et al.*, ‘EFSUMB Technical Review - Update 2023: Dynamic Contrast-Enhanced Ultrasound (DCE-CEUS) for the Quantification of Tumor Perfusion’, *Ultraschall in der Medizin* , vol. 45, no. 1, pp. 36–46, Feb. 2023, doi: 10.1055/A-2157-2587.

[20] V. Rafailidis, A. Charitanti, T. Tegos, E. Destanis, and I. Chryssogonidis, ‘Contrast-enhanced ultrasound of the carotid system: a review of the current literature’, *J Ultrasound*, vol. 20, no. 2, pp. 97–109, Jun. 2017, doi: 10.1007/s40477-017-0239-4.

[21] J. Wang, X. Li, Z. Zhang, C. Jing, and J. Li, ‘Clinical Research of Combined Application of DCEUS and Dynamic Contrast-Enhanced MSCT in Preoperative cT Staging of Gastric Cancer’, *J Oncol*, vol. 2021, Oct. 2021, doi: 10.1155/2021/9868585.

[22] M. L. Izamis, A. Efstathiades, C. Keravnou, E. L. Leen, and M. A. Averkiou, ‘Dynamic contrast-enhanced ultrasound of slaughterhouse porcine livers in machine perfusion’, *Ultrasound Med Biol*, vol. 40, no. 9, pp. 2217–2230, Sep. 2014, doi: 10.1016/J.ULTRASMEDBIO.2014.03.031.

[23] A. L. Emanuel, R. I. Meijer, E. van Poelgeest, P. Spoor, E. H. Serné, and E. C. Eringa, ‘Contrast-enhanced ultrasound for quantification of tissue perfusion in humans’, *Microcirculation*, vol. 27, no. 1, Jan. 2020, doi: 10.1111/MICC.12588.

[24] Siemens Medical Solutions USA, ‘ACUSON S1000 ACUSON S2000 ACUSON S3000 Diagnostic Ultrasound System Instructions for Use’, *User Manual*. 2017.

[25] S. Turco, P. Chen, A. Lyshchik, A. El Kaffas, and M. Mischi, ‘Ultrasound contrast agents: microvascular characterization’, in *Hemodynamic Quantifications By Contrast-Enhanced Ultrasound*, 2023. Accessed: Feb. 05, 2024. [Online]. Available: https://pure.tue.nl/ws/portalfiles/portal/297639802/20230602_Chen_P._hf.pdf

[26] S. Turco *et al.*, ‘Contrast-Enhanced Ultrasound Quantification: From Kinetic Modeling to Machine Learning’, *Ultrasound Med Biol*, vol. 46, no. 3, pp. 518–543, Mar. 2020, doi: 10.1016/j.ultrasmedbio.2019.11.008.

[27] T. Payen *et al.*, ‘Echo-Power Estimation from Log-Compressed Video Data in Dynamic Contrast-Enhanced Ultrasound Imaging’, *Ultrasound Med Biol*, vol. 39, no. 10, pp. 1826–1837, Oct. 2013, doi: 10.1016/J.ULTRASMEDBIO.2013.03.022.

[28] M. Versluis, E. Stride, G. Lajoinie, B. Dollet, and T. Segers, ‘Ultrasound Contrast Agent Modeling: A Review’, *Ultrasound Med Biol*, vol. 46, no. 9, pp. 2117–2144, Sep. 2020, doi: 10.1016/J.ULTRASMEDBIO.2020.04.014.

[29] D. P. Duncan and M. Baillie, ‘Contrast-enhanced Ultrasound Imaging ACUSON Sequoia ultrasound system’. Siemens Medical Solutions USA.

[30] M. He *et al.*, ‘Time-intensity Curve Analysis of Hepatocellular Carcinoma using Two Contrast-enhanced Ultrasound Methods: Contrast Pulse Sequencing and Contrast Harmonic Imaging’, *Advanced Ultrasound in Diagnosis and Therapy*, vol. 4, no. 3, pp. 217–222, Aug. 2020, doi: 10.37015/AUDT.2020.200007.

[31] M. Lampaskis and M. Averkiou, ‘Investigation of the relationship of nonlinear backscattered ultrasound intensity with microbubble concentration at low MI’, *Ultrasound Med Biol*, vol. 36, no. 12, pp. 306–3112, Feb. 2010, doi: 10.1016/j.ultrasmedbio.2009.09.011.

[32] H. Haghi, A. J. Sojahrood, and M. C. Kolios, ‘Collective nonlinear behavior of interacting polydisperse microbubble clusters’, *Ultrasonics Sonochemsitry*, vol. 58, Nov. 2019, doi: 10.1016/j.ultsonch.2019.104708.

[33] J. S. Allen, D. E. Kruse, P. A. Dayton, and K. W. Ferrara, ‘Effect of coupled oscillations on microbubble behavior’, *J Acoust Soc Am*, vol. 114, no. 3, pp. 1678–1690, Sep. 2003, doi: 10.1121/1.1600721.

[34] ‘VueBox Quantification-toolbox’. Bracco Suisse SA, 2023. [Online]. Available: www.bracco.com

[35] M. E. Krommendijk, ‘An ex-vivo perfused porcine liver for magnetic resonance imaging - A master thesis’, 2022. Accessed: Feb. 05, 2024. [Online]. Available: https://essay.utwente.nl/view/programme/66226.html

[36] N. G. Rognin, P. Frinking, M. Costa, and M. Arditi, ‘In-vivo Perfusion Quantification by Contrast Ultrasound:Validation of the Use of Linearized Video Data vs. Raw RF Data’, in *IEEE International Ultrasonics Symposium*, Aug. 2008. doi: 10.1109/ULTSYM.2008.0413.

[37] Klazina Kooiman *et al.*, ‘Ultrasound-Responsive Cavitation Nuclei for Therapy and Drug Delivery’, *Ultrasound Med Biol*, vol. 46, no. 6, pp. 1296–1325, Jun. 2020, doi: 10.1016/j.ultrasmedbio.2020.01.002.

[38] P. J. O’connor *et al.*, ‘Feasibility of Yttrium-90 Radioembolization Dose Calculation Utilizing Intra-procedural Open Trajectory Cone Beam CT’, *Cardiovasc Intervent Radiol*, vol. 43, no. 2, pp. 295–301, Feb. 2020, doi: 10.1007/s00270-019-02198-6.

[39] M. Martin *et al.*, ‘Comparison of perfused volume segmentation between cone-beam CT and 99m Tc-MAA SPECT/CT for treatment dosimetry before selective internal radiation therapy using 90 Y-glass microspheres’, *Diagn Interv Imaging*, vol. 102, pp. 45–52, Jan. 2020, doi: 10.1016/j.diii.2020.09.003.

[40] R. Taiji *et al.*, ‘A novel method for predicting hepatocellular carcinoma response to chemoembolization using an intraprocedural CT hepatic arteriography-based enhancement mapping: a proof-of-concept analysis’, *Eur Radiol Exp*, vol. 7, no. 1, pp. 1–11, Dec. 2023, doi: 10.1186/s41747-022-00315-8.

[41] T. J. Snoeijink, T. G. Vlogman, J. Roosen, E. Groot Jebbink, K. Jain, and J. F. W. Nijsen, ‘Transarterial radioembolization: a systematic review on gaining control over the parameters that influence microsphere distribution’, *Drug Deliv*, vol. 30, no. 1, p. 2226366, Dec. 2023, doi: 10.1080/10717544.2023.2226366.

[42] ‘UMC Utrecht verlicht behandeling leverkanker - UMC Utrecht’. Accessed: Jan. 03, 2024. [Online]. Available: https://www.umcutrecht.nl/nieuws/umc-utrecht-verlicht-behandeling-leverkanker

[43] M. M. A. Dietze *et al.*, ‘A compact and mobile hybrid C-arm scanner for simultaneous nuclear and fluoroscopic image guidance’, *Eur Radiol*, vol. 32, no. 1, pp. 517–523, Jan. 2022, doi: 10.1007/S00330-021-08023-4.

[44] M. M. A. Dietze *et al.*, ‘Clinical Demonstration of a Hybrid C-arm Scanner for Simultaneous Fluoroscopic (CBCT) and Scintigraphic (SPECT) Imaging’, in *IEEE Nuclear Sience Symposium*, Feb. 2023. doi: 10.1109/NSSMICRTSD49126.2023.10338547.

[45] Z. Pickell and A. J. Sinusas, ‘Nuclear Cardiac Imaging in the Interventional Suite’, *Curr Cardiol Rep*, vol. 24, no. 3, pp. 261–269, Mar. 2022, doi: 10.1007/s11886-022-01644-1.

[46] J. R. Eisenbrey *et al.*, ‘US-triggered Microbubble Destruction for Augmenting Hepatocellular Carcinoma Response to Transarterial Radioembolization: A Randomized Pilot Clinical Trial’, *Radiology*, vol. 298, no. 2, pp. 450–457, Feb. 2021, doi: 10.1148/RADIOL.2020202321.

[47] M. Krommendijk and J. Van der Hoek, ‘Protocol for perfusing pig livers’. Accessed: Feb. 05, 2024. [Online]. Available: https://m3i.wiki.utwente.nl/doku.php?id=ex-vivo_liver_setup:protocol_for_perfusing_pig_livers

[48] P. Chen *et al.*, ‘In-vitro investigation of the relationship between microvascular structure and ultrasound contrast agent dynamics’, in *IEEE International Ultrasonics Symposium*, Oct. 2019, pp. 403–406. doi: 10.1109/ULTSYM.2019.8926232.

[49] H. Mirgolbabaee *et al.*, ‘Design, fabrication and characterization of a cohort-based averaged flow phantom of the abdominal aortic aneurysm ’, *[Unpublished paper]*.


SKYTRON
TECHMED
CENTRE